



Analogue experiments of salt flow and pillow growth due to basement faulting and differential loading

M. Warsitzka¹, J. Kley², and N. Kukowski¹

¹Friedrich-Schiller-University Jena, Institute for Geosciences, Germany

²Georg-August-University Göttingen, Geoscience Centre, Structural Geology & Geodynamics, Germany

Correspondence to: M. Warsitzka (michael.warsitzka@uni-jena.de)

Received: 23 June 2014 – Published in Solid Earth Discuss.: 17 July 2014

Revised: 14 November 2014 – Accepted: 20 November 2014 – Published: 6 January 2015

Abstract. Salt flow in sedimentary basins is mainly driven by differential loading and can be described by the concept of hydraulic head. A hydraulic head in the salt layer can be imposed by vertically displacing the salt layer (elevation head) or the weight of overburden sediments (pressure head). Basement faulting in salt-bearing extensional basins is widely acknowledged as a potential trigger for hydraulic heads and the growth of salt structures. In this study, scaled analogue experiments were designed to examine the kinematics of salt flow during the early evolution of a salt structure triggered by basement extension. In order to distinguish flow patterns driven by elevation head or by pressure head, we applied a short pulse of basement extension, which was followed by a long-lasting phase of sedimentation. During the experiments viscous silicone putty simulated ductile rock salt, and a PVC-beads/quartz-sand mixture was used to simulate a brittle supra-salt layer. In order to derive 2-D incremental displacement and strain patterns, the analogue experiments were monitored using an optical image correlation system (particle imaging velocimetry). By varying layer thicknesses and extension rates, the influence of these parameters on the kinematics of salt flow were tested. Model results reveal that significant flow can be triggered in the viscous layer by small-offset basement faulting. During basement extension downward flow occurs in the viscous layer above the basement fault tip. In contrast, upward flow takes place during post-extensional sediment accumulation. Flow patterns in the viscous material are characterized by channelized Poiseuille-type flow, which is associated with subsidence in regions of “salt” expulsion and surface uplift in regions of inflation of the viscous material. Inflation of the viscous material eventually leads to the formation of pillow structures adjacent to

the basement faults (primary pillows). The subsidence of peripheral sinks adjacent to the primary pillow causes the formation of additional pillow structures at large distance from the basement fault (secondary pillows). The experimentally obtained structures resemble those of some natural extensional basins, e.g. the North German Basin or the Mid-Polish Trough, and can aid understanding of the kinematics and structural evolution of sedimentary basins characterized by the presence of salt structures.

1 Introduction

Generally, rock salt buried in sedimentary basins behaves as a viscous fluid (Urai et al., 2008; van Keken et al., 1993) and flows according to a pressure gradient. Pressure gradients in a salt layer can be described by the concept of hydraulic head, which depends on the sum of elevation head and pressure head (Kehle, 1988; Hudec and Jackson, 2007). In the case of basement faulting (Fig. 1a), an elevation head can be imposed on the salt layer by vertical displacement of the salt layer itself. An additional pressure head is induced on the salt layer by differential loading due to lateral changes in thickness of the sediments accumulating on the irregular topography of the faulted surface (e.g. Geil, 1991; Hudec and Jackson, 2007; Jackson et al., 1994; Jackson and Vendeville, 1994; Koyi et al., 1993; Koyi and Petersen, 1993; Krzywiec, 2004b; Remmelts, 1995; Stewart et al., 1996; Vendeville et al., 1995).

Previous scaled analogue experiments investigating salt diapirism driven by thick-skinned extension demonstrated that at the beginning discrete basement faulting is balanced

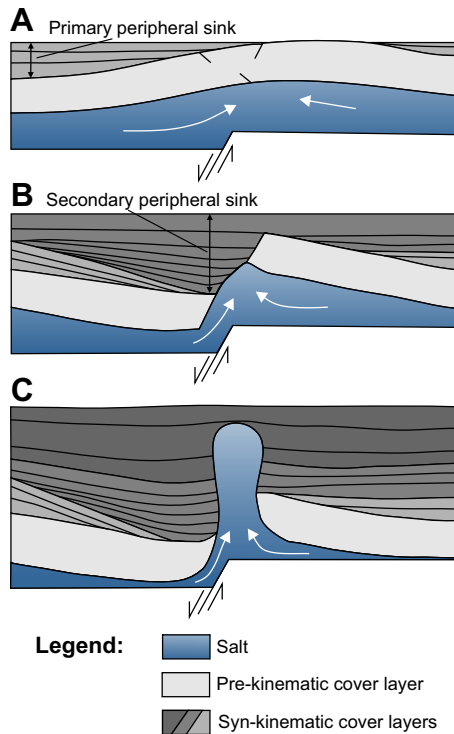


Figure 1. Conceptual model showing the evolution of a salt diapir induced by basement faulting: (a) due to sedimentary loading a salt pillow develops prior to diapiric piercing, (b) further basement extension leads to faulting of the overburden and (c) reactive diapirism. Salt flow is governed by vertical displacement of the salt layer (elevation head) and differential loading due to sediment accumulation in subsiding areas (modified after Koyi et al., 1993).

by flexural bending of the overburden and decoupled by diffuse faulting (Burliga et al., 2012; Dooley et al., 2003, 2005; Ge and Vendeville, 1997; Higgins and Harris, 1997; Jackson and Vendeville, 1994; Koyi et al., 1993; Nalpas and Brun, 1993; Oudmayer and de Jager, 1993; Richard, 1991; Soto et al., 2007; Stephansson, 1972; Vendeville, 1988; Vendeville et al., 1995; Vendeville and Jackson, 1992; Ventissette et al., 2005; Withjack and Callaway, 2000). Deformation within the viscous layer above an active basement normal fault is characterized by flow towards the hanging wall block under sediment-starved conditions. Reverse flow towards the footwall block occurs if sufficient sediment accumulates in the depocentre above the downthrown basement block (Jackson et al., 1994; Koyi et al., 1993; Nalpas and Brun, 1993; Ge and Vendeville, 1997). Furthermore, salt flow into a growing salt structure close to the basement fault can change through time from the footwall side during an early stage to the hanging wall side in a mature stage (Burliga et al., 2012; Koyi et al., 1993). However, in most of these experimental studies finite displacement of the basement faults was large compared to the thickness of the viscous layer. This obscures incremental flow patterns occurring during the early evolution of

salt structures, when offsets of basement faults are still small (Fig. 1).

Therefore, our experimental study is designed to examine incremental strain patterns in a salt layer asserted by both components of the hydraulic head, elevation and pressure head during initiation of a salt structures triggered by basement normal faulting. We purposely divided the experimental procedure into a short pulse of basement faulting and a long phase of post-extensional sedimentation. Furthermore, a sensitivity study was carried out to test the role of characteristic parameters, namely salt thickness, cover thickness and extension rate, in affecting flow patterns and post-extensional structural evolution. A 2-D optical particle tracking system (PIV) was applied to observe incremental particle displacements and strain patterns in both the brittle and the ductile layer during the experiments.

2 Method and procedure

2.1 Scaling analogue experiments

The experiments presented here involve a two-layer ductile-brittle system covering a rigid basement. The viscous near-Newtonian behaviour of rock salt (Urai et al., 2008, van Keken et al., 1993) was simulated by using silicone putty (PDMS, polydimethylsiloxane; dynamic viscosity of 2.3×10^4 Pas at room temperature 20°C and experimental strain rates of $< 10^{-1} \text{ s}^{-1}$; see Appendix A for details). The silicone putty shows a power-law viscous rheology with a low power-law stress exponent ($n = 1.3$; Rosenau et al., 2009) so that it can be regarded as near-Newtonian. Frictional-plastic slip behaviour of overburden sediments is modelled by a granular mixture of quartz sand and PVC microspheres (1 : 1) (see Appendix A for details). This granulate deforms according to the Mohr–Coulomb criterion, a suitable rheology for the simulation of natural sedimentary rocks (e.g. Lohrmann et al., 2003).

For representative quantitative and qualitative information, analogue models have to be scaled geometrically, kinematically and dynamically (Hubbert, 1937; Ramberg, 1967). This requires dimensionless ratios relating the rheologies and stresses of nature to be similar to those for experiments. Referring to previous studies, we employ a geometric scaling factor $1 \times$ of about 10^{-5} , which means 1 cm in the model is equivalent to about 1 km in nature (Koyi et al., 1993; Nalpas and Brun, 1993; Ge and Vendeville, 1997; Withjack and Callaway 2000; Dooley et al. 2003). Dynamical scaling is ensured if force ratios and length ratios are similar (gravitational acceleration = 9.81 ms^{-2}). The reliability of modelling results strongly depends on mechanical coupling between viscous layer and overburden and, therefore, on the ratio between brittle yield strength S_b and ductile strength S_d (see Appendix B for a detailed description of the scaling procedure). Calculation of this strength ratio results in the

following values (Table 1):

$$S_b / S_d (\text{nature}) = \sim 100 - 1000 \quad (1)$$

and

$$S_b / S_d (\text{model}) = 50 - 180. \quad (2)$$

The model ratio lies within the lower range of the natural ratio. Hence, the models can be considered as dynamically scaled. Scaling of time can be achieved by dividing the viscosity ratio η^* through the normal stress ratio σ_N^* (see Appendix B). The resulting time scaling factor $t^* = \sim 10^{-10}$ means that 1 h in the experiment equals ~ 1 Ma in nature.

Note that the applied scaling procedure is subject to high uncertainties, since especially salt viscosity and strain rate during salt flow are not well constrained and can vary over 2–3 orders of magnitude (Jackson and Talbot, 1986). Nevertheless, similar analogue materials and length ratios have been used for decades and found suitable for modelling of salt tectonic processes (see references above).

The mixture of quartz sand and PVC beads possesses slightly lower frictional properties ($\varphi \sim 27^\circ$), but also a lower bulk density ($\rho_b = 1300 \text{ kg m}^{-3}$) than pure quartz sand ($\rho_b = 1580\text{--}1710 \text{ kg m}^{-3}$) (see Appendix A). By applying a low density contrast between cover and viscous layer in our experiments (300 kg cm^{-3}), buoyancy forces are not overestimated (Allen and Beaumont, 2012). Thus, we intend to ensure a more realistic stress relation during early stages of salt pillow development, and closer similarity to natural shallow (~ 1000 m), partly compacted sediments, which also possess densities lower or slightly higher than salt.

2.2 Experimental set-up

In this generic experimental study, we intend to simulate conditions of salt structure evolution during the onset of basement extension. In many rifts and intracontinental basins multiple extensional phases alternate with phases of tectonic quiescence as revealed by structural analysis or subsidence patterns (e.g. Alves et al., 2002; Jackson and Vendeville, 1994; Kockel, 2002; Mohr et al., 2005; van Wees et al., 2000). Therefore, the experimental procedure applied here assumes a relatively short extensional pulse followed by a longer phase of tectonic quiescence accompanied by sedimentation. In order to monitor the characteristic deformation patterns in both phases, we artificially separated basement extension and sedimentation in the experimental procedure. Furthermore, the salt layer in many extensional basins is overlain by more or less isopachous overburden before basement extension and salt movement begins (e.g. Alves et al., 2002; Baldschuhn et al., 2001; Duffy et al., 2013; Remmelts et al., 1995). Thus, we introduced an initial cover layer of uniform thickness in each experiment, which is here referred to as “pre-kinematic cover layer”.

Appropriate experimental values for e.g. layer thicknesses, displacement of the basement faults or the duration

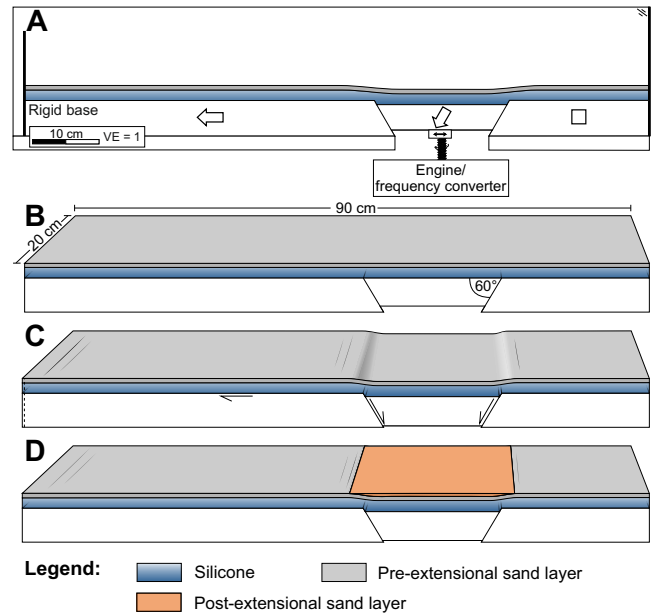


Figure 2. (a) Side view of experimental box comprising analogue materials silicone and granulate as well as subdivided rigid basement. Basal displacement is driven by a controlled engine. (b) In general the model procedure starts with a planar layer configuration. (c) Basal displacement is applied. (d) Surface depressions are filled with sifted granulate. Sieving procedure is repeated daily.

of extension are adapted to the conditions of the Central European Basin system, which contains prominent extensional segments (e.g. Central Graben, Horn Graben, Mid-Polish Trough) (Ziegler, 1982) and numerous salt structures (Maystrenko et al., 2013). Here, the pre-extensional overburden thickness h_b varies from a few hundred metres (Mid-Polish Trough; Krzywiec, 2004a) to ~ 1000 m (North German Basin; Baldschuhn et al., 2001; Maystrenko et al., 2013; Scheck et al., 2003). The maximum original salt layer thickness h_d in the centre of extensional basins mainly lies between 1000 m (Northeast German Basin) and 1500 m (Mid-Polish Trough), but can attain 3500 m (Central North German Basin; Frisch and Kockel, 1999; Maystrenko et al., 2013). Hence, a ratio of overburden thickness to salt thickness of $H_r < 1$ is a reasonable assumption. Throughout this paper, we define small-offset displacement at the basement fault as being considerably smaller than the thickness of the salt layer. Thus, the ratio D_r of basement fault offset d to thickness of the salt layer h_d can also be assumed to be < 1 .

Experiments were performed in a 90×20 cm wide glass-sided box (Fig. 2a). The rigid base is subdivided into three blocks by two opposite planes dipping 60° . The right block is fixed, the middle one subsides controlled by an engine and the left one is free to move horizontally. The left block is wider in order to investigate the post-extensional model evolution at distance from the basal faults. The initially planar

Table 1. Scaling parameters. Material properties (density, viscosity, friction and cohesion) are stated for analogue materials used in this experimental study (Appendix A).

Parameter	Sign	Dimension	Model	Nature	Scaling factor (model/nature)	Reference for natural values
Geometric	l^*	[m]	0.01	1000	$\sim 10^{-5}$	
Thickness (ductile layer)	h_d	[m]	0.01–0.02	1400–2500	10^{-5}	Kockel (2002); Maystrenko et al. (2013); Nalpas and Brun (1993); Scheck et al. (2003)
Thickness (brittle layer)	h_b	[m]	0.003–0.015	600–1200	10^{-5}	Nalpas and Brun (1993)
Kinematic						
Strain	ε	–			1	–
Time	t	[s]	$100h = 10^5 s$	$\sim 30 Ma = \sim 10^{15}$	10^{-10}	–
Extension rate	u	$[m s^{-1}]$	10^{-6}	$1 mm a^{-1} = \sim 10^{-11} m s^{-1}$	$\sim 10^5$	Allen and Allen (2005)
Strain rate in viscous layer	ε'	$[s^{-1}]$	$\sim 10^{-5}$	$10^{-11}–10^{-15}$	$10^{-6}–10^{-10}$	Jackson and Talbot (1986); Nalpas and Brun (1993)
Dynamic						
Gravity acceleration	g	$[m s^{-2}]$	9.81	9.81	1	–
Density (ductile layer)	ρ_d	$[kg m^{-3}]$	970	2200	0.44	Jackson and Talbot (1986)
Density (brittle layer)	ρ_b	$[kg m^{-3}]$	1220	1800–2500	0.52–0.72	Jackson and Talbot (1986)
Dynamic viscosity (ductile layer)	η	[Pa s]	2.3×10^4	$10^{17}–10^{19}$	$\sim 10^{-14}$	Nalpas and Brun (1993)
Internal peak friction coefficient	μ	–	0.51 (± 0.006)	0.5–0.6	1	Weijermars et al. (1993)
Internal friction angle	ϕ	[°]	27	~ 30		Weijermars et al. (1993)
Cohesion [Pa]	C_0	[Pa]	~ 100	5×10^6		Byerlee (1978)
Stress and pressure		[Pa]			$\sim 10^{-5}$	–
Brittle strength	S_b	[Pa]	60–160	$\sim 10^7$	$\sim 10^{-5}$	–
Ductile strength	S_d	[Pa]	0.5–2	$\sim 10^5$	$\sim 10^{-5}$	–
Brittle strength/ductile strength	S_b/S_d	–	50–180	$\sim 100–1000$	~ 1	–

base is covered with a flat layer of silicone putty as well as a pre-kinematic granular layer (Fig. 2b).

Each experiment starts with a displacement of the basal plate (extensional phase), whereby the middle block is pulled down $d = \sim 6–7$ mm (Fig. 2c), which causes ~ 7 mm lateral stretching of the whole model ($\sim 0.8\%$). The displacement rate e on the normal faults of the basal plate ranges from 0.6, 4 to $20 mm h^{-1}$, which represents a natural extension rate of 0.05 to $2 mm a^{-1}$ (50 to $2000 m Ma^{-1}$). According to our scaling, the duration of the extensional phase (0.3 to 10 h) is about 0.3 to 11 Ma, which are reasonable values for a short extensional pulse, as occurred e.g. in the North German Basin (e.g. Kockel, 2002). After termination of basal displacement, accumulation of additional sand was delayed another 15 min in order to record the post-extensional strain patterns. After this interim period additional sand (post-extensional layers) was sieved into topographic depressions to apply a pressure head on the viscous layer (Fig. 2d) (syn-sedimentary phase). The sieving procedure was repeated every day. The average sedimentation rate was $\sim 5 mm d^{-1}$ depending on the depth of the depressions. This rate represents a natural sedimentation rate of $\sim 0.002 mm a^{-1}$ ($\sim 20 m Ma^{-1}$), which is 1 order of magnitude lower than the average extension rate. Since we intended to investigate post-extensional structural evolution with realistic initial density contrasts, the syn-sedimentary phase lasted much longer than the extensional phase (> 5

days equivalent up to > 100 million years in nature). In nature, sediment compaction would lead to an increase of the cover density and, therefore, to a faster growth of the salt structures during (see discussion).

In total, 12 experiments were carried out (Table 2). In order to examine sensitivity on the boundary conditions and reproducibility of the experiments, a reference experiment with equal initial conditions was repeated four times (Exp. 1a–c). The early phase was identical for these three experiments, although some variations were introduced at a later stage. In Exp. 1b, an additional phase of basal displacement was applied after 10 days. Exp. 1c was terminated earlier to observe intermediate structures. In additional experiments (Exp. 2–8) initial parameters (layer thicknesses and displacement rates) were changed systematically to test their influence on structural evolution and kinematics (Table 2). In Exp. 4b, sand accumulation was applied simultaneously with displacement of the basal plate.

We used coloured sand layers to track the structural evolution. On the basis of digitized photographs of cross-sections, the final structures were sequentially restored using a vertical-simple shear restoration algorithm (Rowan and Ratliff, 2012) in 2-D Move (Midland Valley). Furthermore, 3-D models were constructed in 3-D Move (Midland Valley).

A computer-based displacement data analysis (particle imaging velocimetry, PIV) tool provided by StrainMaster[®] (La Vision GmbH, 2002) was used to monitor incremental

Table 2. Experiments and key parameters, where h_d is the thickness of the ductile silicone and h_b the thickness of the brittle sand cover.

Experiment	h_d [cm]	h_b [cm]	Extension rate e [mm h ⁻¹]	Subsidence d [mm]	Total duration [days]	PIV monitoring	Comment
1a	1.5	0.6	4	6	12	side view	–
1b	1.5	0.6	4	6+6	18	side view	two phases of extension
1c	1.5	0.6	4	6	18	side view	
1d	1.5	0.6	4	6	4	side view + top view	–
2	1.5	0.6	20	6	4	side view	–
3	1.5	0.6	0.6	6	4	side view	–
4a	1	0.6	4	6	8	side view	–
4b	1	0.6	4	6	8	side view	sand accumulation during basement extension
5	2	0.6	4	6	9	side view	–
6	1.5	0.4	4	6	9	side view	–
7	1.5	1	4	6	5	side view	–
8	1.5	1.5	4	6	6	side view	–

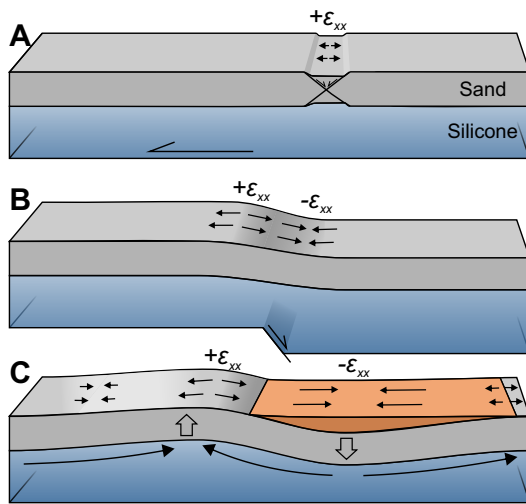


Figure 3. Explanation of lateral strain observed with PIV in top view (see results). (a) Cover extension, which is due to displacement of the basement, is measured as positive lateral strain ($+\epsilon_{xx}$). (b) Layer bending due to extensional forced folding is accompanied by extension ($+\epsilon_{xx}$) and compression ($-\epsilon_{xx}$) of the sand surface. (c) Similarly, surface uplift due to silicone inflation leads to crestal extension ($+\epsilon_{xx}$). Surface subsidence due to silicone deflation causes compression ($-\epsilon_{xx}$).

strain in the granular and viscous layers, respectively, during the experiment. PIV is an optical, non-intrusive method for particle tracking consisting of digital 12-bit monochrome CCD (charge-coupled device) cameras (4 Mega Pixel; ~ 20 pixels cm^{-1}) and analysis software (LaVision 7.0). Images were taken every minute during the extensional phase and every 3 minutes during the syn-sedimentary phase. This is sufficient to follow deformation under low experimental strain rates. The images were processed with a cross-correlation algorithm calculating translation and distortion of textural differences (i.e. grey values) between two sequen-

tial images with a predefined time difference (Adam et al. 2005). Depending on the optical resolution of the cameras and the precision of the cross-correlation algorithm used, a spatial resolution < 0.1 pixels can be achieved (Adam et al., 2005). The resulting accuracy of the displacement vector is $\delta d \approx 0.05$ mm for an assumed box width of 90 cm. On the basis of the calculated incremental vector displacement field, cumulative displacement, x - and y -component of displacement or strain tensor components (e.g. normal strain ϵ_{xx} and shear strain ϵ_{xy}) as well as long-term average flow velocities u can be calculated. To achieve a textural pattern in the transparent silicone, it was blended with a small amount of sand particles (~ 10 g sand per 1 kg silicone). The effect of this impurity on density or viscosity of the silicone is negligible (Boutelier et al., 2008; Warsitzka et al., 2013).

All experiments were monitored in 2-D side view, which provides strain patterns in the viscous layer close to the glass wall. This monitored strain can be assumed to be representative for strain occurring in the centre of the box at least during early stages of the experiment when deformation of the cover is similar between the centre and the edges of the box. During later stages of the experiment, flow patterns in the centre of the box are no longer parallel to the glass walls. Thus, strain patterns observed at the glass wall can merely provide rough estimations of strain occurring in the interior of the box. The Exp. 1c was additionally recorded in 2-D top view to observe lateral deformation on the sand surface. For analysis of flow kinematics, the horizontal displacement d_x in side view or normal strain ϵ_{xx} in top view was used. The 2-D top view shows lateral extensional ($+\epsilon_{xx}$) or compressional strain ($-\epsilon_{xx}$). This strain can be initiated for instance by thin-skinned extension of the sand cover (Fig. 3a). Furthermore, flexural bending of the sand produces extensional, as well as compressional domains at the sand surface (Fig. 3b). Similarly, it is possible to identify uplifting and subsiding areas in the sand layer due to silicone flow (Fig. 3c). Strain distribution in a folded layer is characterized

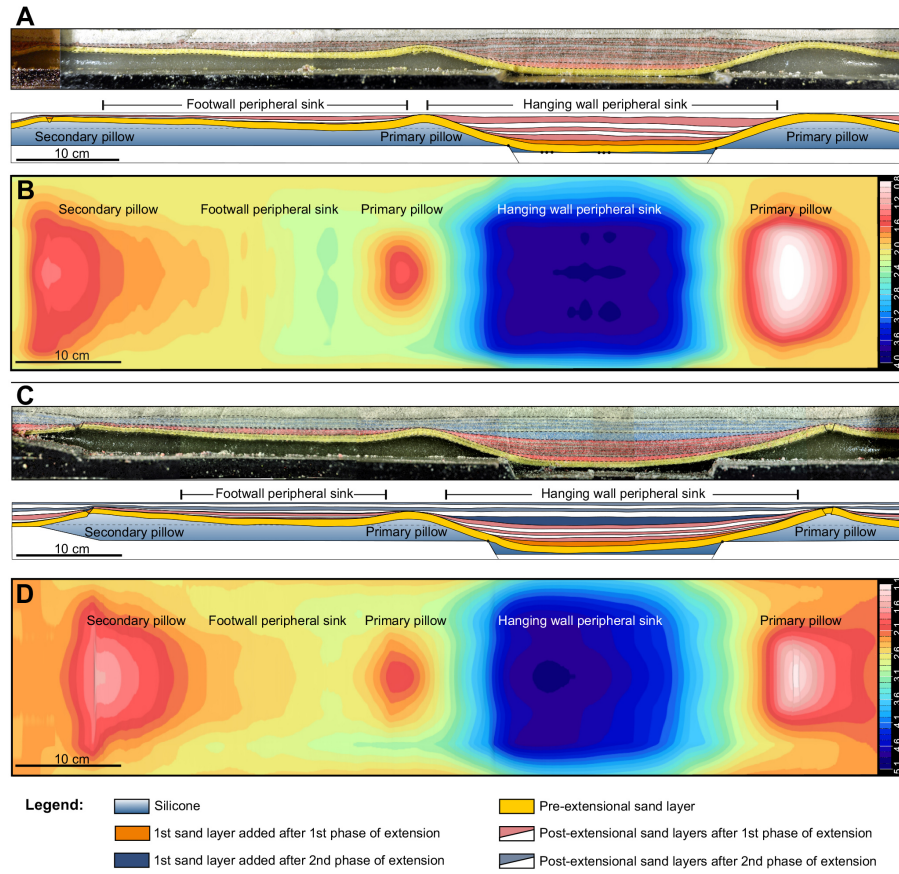


Figure 4. (a) Cross-section of reference Exp. 1a after 12 days. Post-extensional strata reveal the hanging wall peripheral sink (HPS) enclosed by two pillow-like silicone elevations. Additional sinks as well as an additional secondary pillow occur on the left side of the box. (b) Colour map displaying the depth of the top of the silicone layer related to the final surface from Exp. 1a. The diameters of the pillows are smaller than the diameter of the HPS. (c) Cross-section of reference Exp. 1b after 18 days, in which an additional phase of extension was applied after 10 days. The crests of the pillows are slightly faulted. (d) Depth map of the top of the silicone layer from Exp. 1b showing that the pillow structures are asymmetric.

by crestral stretching ($+\varepsilon_{xx}$) of the sand surface in anticlines, whereas synclinal bending is associated with compressional strain ($-\varepsilon_{xx}$) (Schultz-Ela and Jackson, 1996).

Strain monitoring with PIV is non-intrusive (Adam et al., 2005), i.e. only the strain at the model surface can be observed. This restricts monitoring of movement in the silicone, which is constrained by friction on the glass wall boundaries and, therefore, not plane-strain. Thus, displacement observed at the glass wall is merely a fractional amount of displacement, which takes place in the middle of the box (Warsitzka et al., 2013). We reduced the effect of lateral friction of viscous material on the glass walls by lubricating the glass with a thin film of glycerine. Due to this the silicone is able to easily slide along the side walls during the experiment, which improves strain monitoring by PIV. Without such lubrication, strain in the silicone layer would only take place at some distance from the glass walls.

3 Experimental results

3.1 Experimental structures

Cross-sections through the centre of the box of reference experiments 1a and 1b (Fig. 4a, c) show the final structures obtained after 12 days or 18 days, respectively. A peripheral sink with thickened sand layers developed above the down-thrown hanging wall basement block. This sink is here called the hanging wall peripheral sink (HPS). It is bounded by two pillows at several centimetres distance from the basement faults. The post-extensional sand layers (red/white; blue/white) pinch out towards the crests of the two pillows causing a bowl-shaped structure of the HPS. The width of the HPS is larger than the width of the underlying basement graben. The silicone beneath the HPS is depleted, which eventually brings the base of the sand in contact with the edges of the basement footwall blocks.

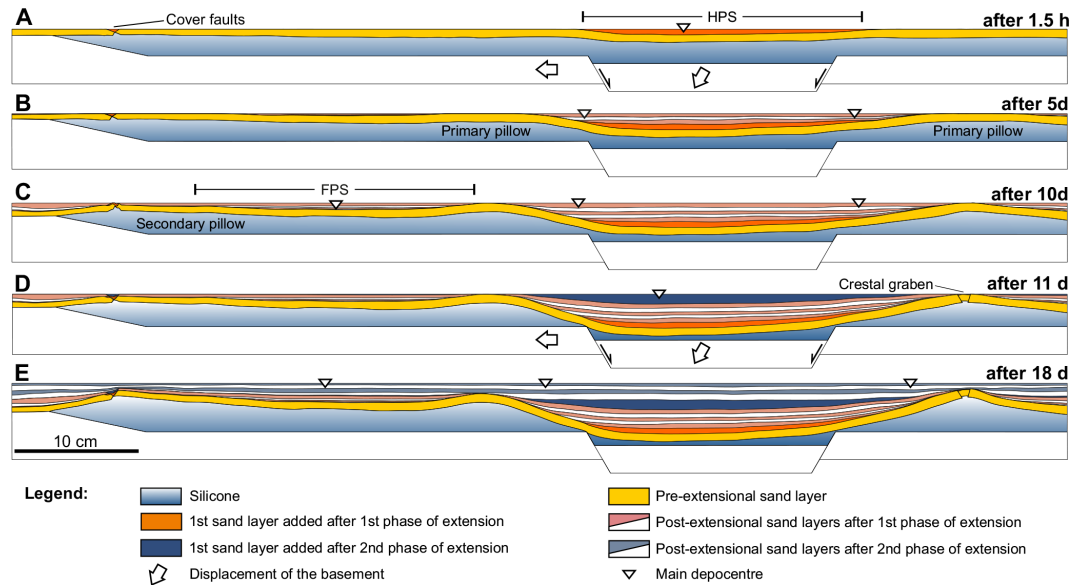


Figure 5. Restoration of final cross-section of Exp. 1b. (a) At the end of basement extension the hanging wall peripheral sink (HPS) begins to subside. (b) Additional sand accumulated causes the formation of pillow structures close to downthrown basement block as well as above the platform at the left side of the box (secondary pillow). (c) The subsidence during the second phase of basement extension is marked by the dark blue layer. (d) Further post-extensional sand accumulation (blue/white) increases the elevation of the pillow-like structures.

Two types of pillow-like structures can be distinguished in the experiments. The first (primary pillows) are situated adjacent to the basement fault above the footwall block. The second type (secondary pillow) is located on the footwall platform near the left-hand end of the experimental box. Depth maps of the top of the viscous layer (Fig. 4b, d) reveal that the pillows are elongated and their long axes trend parallel to the basement offset. An additional peripheral sink (footwall peripheral sink) containing thickened post-extensional layers is located between the left-hand primary pillow and the secondary pillow.

In Exp. 1b the basement was displaced a second time, which is marked by the blue/white layers. Here, the pre-kinematic sand layer (yellow) displays minor faulting at the crest of the pillows. Post-extensional layers of the first phase (red/white) are bent upward. Different from Exp. 1a, the silicone layer beneath the HPS is not completely depleted.

3.2 Evolution of experimental salt structures

The structural evolution of Exp. 1b is illustrated by means of restorations of the central cross-section shown in Fig. 4. During the first syn-extensional stage, a small depression (HPS) forms due to subsidence of the central basement block (Fig. 5a). The cover layer above each fault tip is bent into a monocline roughly 5 cm wide above a ductile layer that began 1.5 cm thick. Lateral extension in the cover layer is mainly balanced by peripheral cover grabens near the left edge of the box. These cover grabens are located close to the region where the silicone pinches out due to a basement

wedge, and can be regarded as an edge effect. During the syn-sedimentary stage, surface depressions were filled by adding sand. The first post-extensional sand layer (orange) represents the surface subsidence due to basement displacement. Successive growth beds (red–white) reflect downwarping due to flow of the viscous material. After several phases of sand accumulation and accompanying expulsion of the silicone, the HPS widens significantly (Fig. 5b). Areas of maximum sand accumulation gradually move from the centre of the HPS towards the rising pillow crests. On the outer side of the left-hand primary pillow, an additional peripheral sink (FPS) develops. Eventually, a secondary pillow evolves above the left footwall block (Fig. 5c).

During the second pulse of rapid extension with additional 6 mm of displacement along the basement faults (displacement rate = 4 mm h^{-1}) (Fig. 5d), the subsidence of HPS increased. This leads to a contact of the base of the HPS with the edges of the footwall blocks. Consequently, no additional silicone is expelled from the hanging wall side and the depocentres move closer to the crests of the pillows (Fig. 5e). During successive post-extensional sand accumulation (blue–white), the primary pillow structures become more pronounced and elevated (Fig. 5e). The growth of the secondary pillow accelerates with increased subsidence of the footwall peripheral sink.

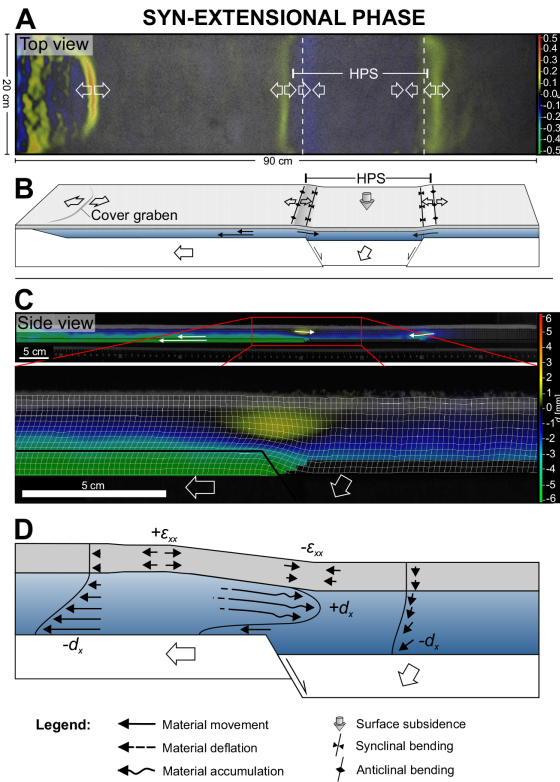


Figure 6. Results of PIV monitoring during syn-extensional phase of the reference experiments 1b and Exp. 1c. **(a)** Top view of Exp. 1c: lateral strain ϵ_{xx} observed with PIV displaying zones of extension (yellow) and zones of compression (blue). Dashed lines indicate location of basal faults. HPS = hanging wall peripheral sink. **(b)** Sketch showing the interpretation of the PIV strain patterns. **(c)** Side view of Exp. 1b: horizontal displacement d_x observed with PIV including a detailed view of the left basement fault. Coloured areas display rightward (yellow–red) and leftward (green–blue) movement of the analogue material. **(d)** Conceptual sketch (arrows are not to scale) summarizing the interpreted displacement patterns and showing vector profiles representing the material movement. The viscous material above the fault tip flows towards the hanging wall side opposed to the shearing along the basement.

4 Displacement and strain patterns

Displacements and strain patterns are visualized using PIV monitoring for the phases during basement extension, after termination of basement extension and during accumulation of post-extensional sand layers.

4.1 Syn-extensional phase

Figure 6 shows the displacement and strain patterns of Exp. 1b after 6 mm of vertical basal displacement or 1.5 h, respectively. Patterns of lateral strain (ϵ_{xx}) observed in top view of the sand surface (Fig. 6a) reveal zones of compression ($-\epsilon_{xx}$, blue) and zones of extension ($+\epsilon_{xx}$, red). High-

est amounts of ϵ_{xx} are accommodated at a cover graben at the left side of the box in an extensional zone. Less pronounced zones of extensional strain occur adjacent to the basement faults. These zones are surrounded by two compressional zones above the edges of the hanging wall basement block. The extensional domains bordering the basement faults above the footwall blocks are the combined effect of bending of the cover (see explanation in Fig. 3) and lateral stretching due to opposite movement in the silicone (Fig. 6b). Similarly, the less pronounced compressional domains above the hanging wall block result from layer bending.

In the side view of Exp. 1b, horizontal displacement d_x illustrates the lateral movement of the left basement block (Fig. 6c). The amount of d_x decreases vertically within the viscous silicone layer and virtually drops to zero in the sand layer. Hence, shearing at the base is not transmitted into the cover. As indicated by the vector grid these strain patterns in the viscous layer can be described as shear flow (Couette flow). Additionally, significant horizontal movement in the silicone can be recognized directly above the fault tip in a 3–4 cm wide, elliptical zone. Although the silicone layer is sheared in the opposite direction by the leftward moving basement block, silicone flows towards the subsiding basement block (Fig. 6c). The vector grid in this elliptical zone shows a vertically parabolic shape, which is characteristic for channelized Poiseuille-type flow.

4.2 Post-extensional phase

After basement extension had been stopped, deformation was monitored for approximately 15 min, before the first post-extensional sand layer was added. During this interim period, patterns of the lateral strain ϵ_{xx} observed in top view of Exp. 1b (Fig. 7a, b) show extensional domains (yellow) at the edges of the central hanging wall block and at the peripheral cover graben. Zones of compressional strain (blue) are identified at the edges of the footwall blocks, in the centre of the hanging wall block and adjacent to the peripheral cover graben. As explained by means of Fig. 3, extensional strains can be attributed to uplift and anticlinal bending of the thinned cover, whereas areas of compressional strain indicate subsidence and synclinal bending of the cover. Hence, the surface subsides at the edges of the footwall blocks, whereas it is uplifted at the edges of the hanging wall block. Meanwhile the peripheral cover graben is uplifted, whereas adjacent areas subside. Complex strain patterns above the centre of the left footwall block are a result of slightly irregular thicknesses of the sand layer. The amount of strain (max. 0.025 %) is one order of magnitude lower than strain during the syn-extensional phase (max. 0.5 %).

The side view of Exp. 1b (Fig. 7c) reveals flow of the viscous material towards the subsided basement block. The zones of downward flow are roughly 6 cm wide, as identified through the coloured area. Therefore, this zone is twice as wide as in the syn-extensional stage. The vector grid allows

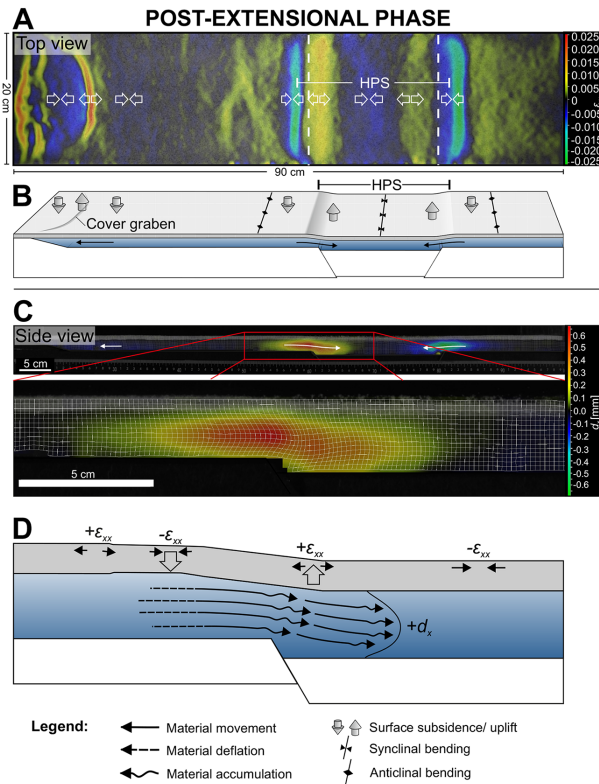


Figure 7. Results of PIV monitoring during the post-extensional phase of the reference experiments 1b and Exp. 1c 15 min after basement extension had ceased. **(a)** Top view of Exp. 1c: lateral strain ϵ_{xx} observed with PIV displaying zones of extension (yellow) and zones of compression (blue). Dashed lines indicate location of basal faults. HPS = hanging wall peripheral sink. **(b)** Sketch showing the interpretation of the PIV strain patterns. **(c)** Side view of Exp. 1b: horizontal displacement d_x observed with PIV including a detailed view of the left basement fault. Coloured areas display rightward (yellow–red) and leftward (green–blue) movement of the analogue material. **(d)** Conceptual sketch (arrows are not to scale) summarizing the interpreted displacement patterns and showing representative vector profiles of the material movement.

identification of a vertically parabolic shape of the vector profile occurring in the region of active flow. The viscous material is mainly accumulated directly above the fault step and above the hanging wall block, which can be inferred by the horizontally compressed vector grid. Maximum displacement d_{xmax} in the silicone ranges between 0.6 and 0.7 mm in the 15 min of this interim period. Hence, maximum displacement rates u achieved by viscous flow are 2.4 to 2.8 mm h⁻¹, which is nearly twice as high as during the syn-extensional phase ($u = \sim 1.5$ mm h⁻¹).

The summarizing sketch (Fig. 7d) explains how the zones of silicone expulsion correspond to areas of lateral cover compression ($-\epsilon_{xx}$) in the cover layer. The zone where silicone is accumulated is related to surface extension ($+\epsilon_{xx}$) (Fig. 7d). This indicates that down-slope silicone flux above

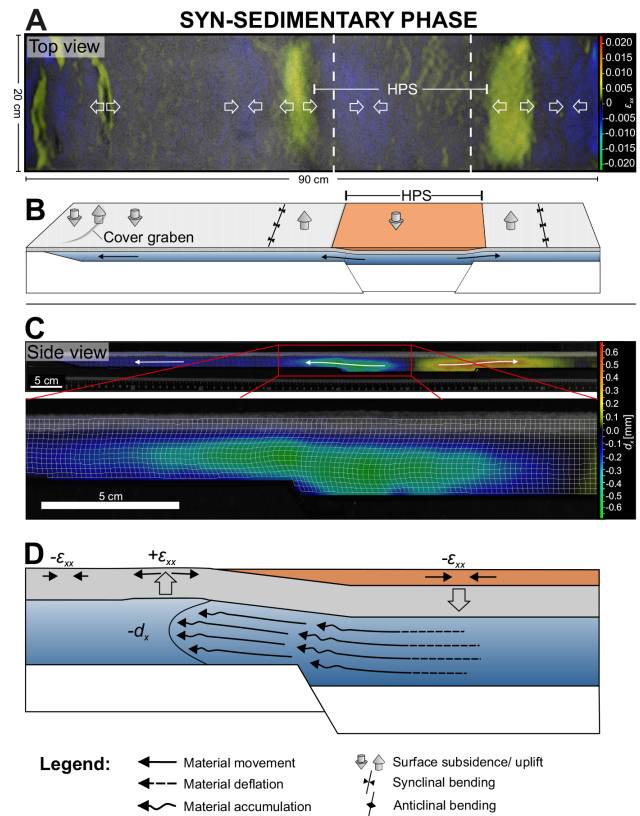


Figure 8. Results of PIV monitoring during syn-sedimentary phase of the reference experiments 1b and Exp. 1c 1h after addition of the first post-extensional sand layer. **(a)** Top view of Exp. 1c: lateral strain ϵ_{xx} observed with PIV displaying zones of extension (yellow) and zones of compression (blue). Dashed lines indicate location of basal faults. HPS = hanging wall peripheral sink. **(b)** Sketch showing the interpretation of the PIV strain patterns. **(c)** Side view of Exp. 1b: horizontal displacement d_x observed with PIV including a detailed view of the left basement fault. Coloured areas display rightward (yellow–red) and leftward (green–blue) movement of the analogue material. **(d)** Conceptual sketch (arrows are not to scale) summarizing the interpreted displacement patterns and showing representative vector profiles of the material movement.

the fault tip entails uplift above the hanging wall block and subsidence above footwall blocks. In the same way, extensional strain observed at the peripheral cover graben denotes uplift. This suggests flow of viscous material towards the thinned cover.

4.3 Syn-sedimentary stage

One hour after filling the surface depressions, zones of extension ($+\epsilon_{xx}$) and compression ($-\epsilon_{xx}$) have developed (Fig. 8a). These zones are wider and the lateral strain (ϵ_{xx}) is more diffuse than in the post-extensional phase. In contrast to the post-extensional phase, slight compression occurs directly above the downthrown basement block. Meanwhile, areas adjacent to the basement fault on the footwall block are

characterized by extension, surrounded by additional zones of compression further outboard. The region around the peripheral cover graben at the left edge of the box displays slight extensional strain. As in the post-extensional stage, these zones of extensional strain and compressional strain can be related to surface uplift or subsidence, respectively, as illustrated in the interpretive sketch (Fig. 8b).

The displacement pattern revealed in side view (Fig. 8c) indicates that the viscous material flows from the down-thrown block towards the footwall blocks. Hence, silicone is expelled from the lowered basement compartment to the higher basement compartments on both sides. The regions in the viscous layer affected by horizontal displacement are wider than in the previous phases. Furthermore, these regions are roughly twice as wide (~ 11 to 13 cm) as the monocline in the cover layer (~ 6 cm). A parabolic-shaped vector grid denotes Poiseuille-type flow within this zone. A horizontally compressed vector grid indicates that viscous material accumulates close to the edge of the basement fault and above the footwall block. The maximal horizontal displacement $d_{x\max}$ in the viscous layer was approximately 0.6 to 0.7 mm during one hour of recording. Thus, displacement rates ($u = 0.6$ to 0.7 mm h⁻¹) were significantly lower than during the post-extensional phase ($u = 2.4$ to 2.8 mm h⁻¹).

Combining the observations from top view and side view, it can again be shown that the zones of silicone expulsion and silicone inflation fit with areas of surface compression or surface extension (Fig. 8d). Hence, horizontal flow in the viscous layer is predominantly compensated by vertical movement in the cover layer. Subsidence of the cover layer on the hanging wall block expels silicone up the basement fault. Consequently, silicone inflation onto the footwall block induces surface uplift adjacent to the basement step. Anticlinal uplift above the footwall blocks (yellow areas) eventually results in the formation of the primary pillow structures (Fig. 4). Furthermore, uplift of the peripheral cover graben continues. Nevertheless, the amount of uplift is less than during the post-extensional phase, which is a result of burial under sand in the centre of the cover graben.

4.4 Subsequent sedimentation phases

During ongoing accumulation of sand, the horizontal flow pattern in the silicone layer changes gradually (Fig. 9). Initially, horizontal flow is restricted to the region above the fault tip (Fig. 9a), while only minor displacement occurs away from the basement fault above the footwall block. Due to subsequent sand accumulation in the HPS, the zone affected by viscous flow above the fault tip widens and migrates away from the basement step along the footwall block (Fig. 9b). After 10 days significant viscous deformation is induced away from the initial basement fault (Fig. 9c). Although the primary pillows are mainly supplied from the area above the hanging wall block, a zone of rightward (yellow) directed flow can be observed. This indicates material in-

flux from the footwall side into the primary pillows, which is driven by the subsidence of an additional peripheral sink (footwall peripheral sink, Fig. 5c). Furthermore, leftward directed displacement (blue) at the left edge of the box increases. This reflects material flow during increased growth of the secondary pillow. At this stage intense flow is active within the entire box. Note that at late stages, silicone flow is no longer parallel to the glass walls. The pillow-like structures developed only in the centre of the experimental box resulting in circular inflow from all sides. Only a part of this flow can be observed at the glass wall boundary.

4.5 Second phase of extension

After 11 days, a second phase of rapid extension with 6 mm of displacement was applied in reference experiment 1b (displacement rate = 4 mm h⁻¹). In general, displacement patterns during this second extensional phase are similar to those observed in the first extensional phase (Fig. 10). Nevertheless, absolute displacement in the silicone layer above the fault tip is larger in the second phase than in the first phase. During the post-extensional and the syn-sedimentary phase, the lateral extent of viscous flow is smaller after the second extensional phase. Furthermore, accumulation of the viscous material predominantly takes place above the footwall side. This indicates that the drainage channel in the silicone layer above the fault tip is reduced due to subsidence of the HPS.

5 Sensitivity study

The structural development and flow kinematics are basically similar in all experiments presented above. However, systematic variations depending on the thickness of the viscous layer h_a , the thickness of the cover layer h_b and the basement displacement rate e can be perceived. A comparison of all experimental cross-sections and displacement patterns occurring in the specific experiments can be found in the Supplement. A summary of these flow patterns for the syn-sedimentary stage, and the maximum flow velocities in the centre of the silicone layer is presented in Fig. 11a–c. Flow velocities u were calculated for the end of the extensional stage (after 1.5 h), the end of the post-extensional stage (after 15 min), and for each syn-sedimentary phase (1 h after accumulation of sand) by dividing the maximum displacement in the centre of the viscous layer by the total time (Fig. 11a–c). In general, displacement rates u are highest during the post-extensional phase ($u = 1$ to 5 mm h⁻¹). Displacement rates during the syn-sedimentary phases are notably lower ($u < 1$ mm h⁻¹). In most experiments, displacement rates increase gradually with each syn-sedimentary phase.

5.1 Effect of basement extension rate e

Slower basement extension causes a wider and smoother bending of the monoclines above the fault tips (Exp. 3;

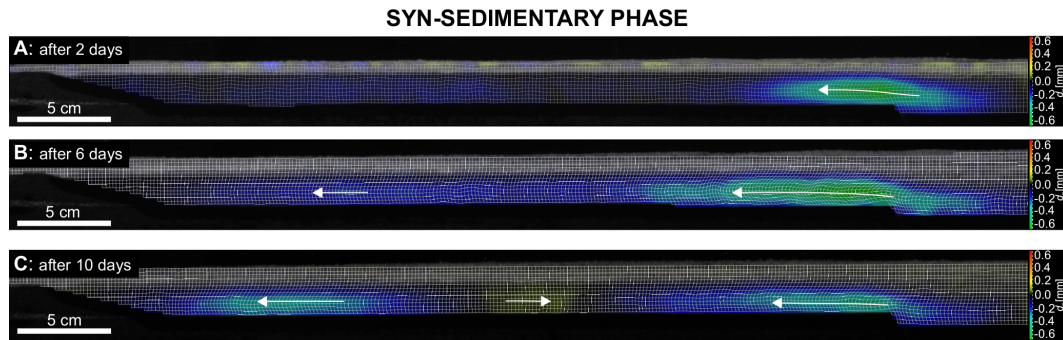


Figure 9. Time series of PIV displacement patterns of the reference experiment Exp. 1b during syn-sedimentary phase. (a) After 2 days, pronounced leftward (blue) directed movement occurs close to the basement fault tip. (b) After 6 days, the zone of leftward movement increases in width and additional flow appears away from the basement fault. (c) After 10 days, significant displacement can still be observed above the basement fault and away from it.

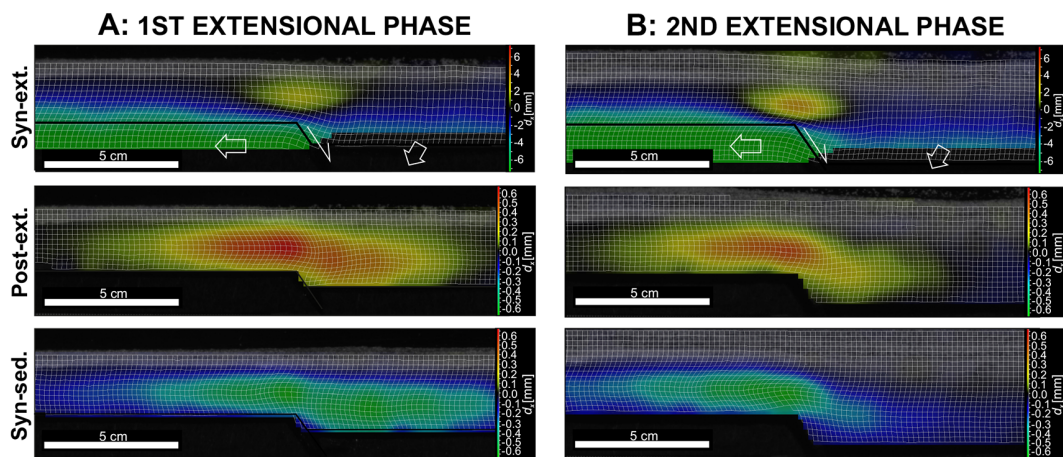


Figure 10. Comparison of horizontal displacement d_x in side view above the tip of the basement fault during (a) first and (b) second phase of basement extension of the reference experiment 1b after 11 days of experimental duration. Coloured areas denote rightward (yellow–red) and leftward (green–blue) movement of the analogue material.

Fig. 11a). Furthermore, the position of the cover graben is located in a greater distance from the basement fault. If e is large (Exp. 2), a comparably narrow monocline and a small cover graben develops adjacent to the basement fault.

During the syn-extensional phase, the zone above the fault tip, which is affected by downward flow, increases in width, if e is small (Fig. 11a). Maximum displacement $d_{x\max}$ in the silicone layer is significantly higher at slow basement extension (Exp. 3: $d_{x\max} = \sim 5$ mm in 495 min) than for rapid basement extension (Exp. 2: $d_{x\max} = \sim 0.5$ mm in 16 min). However, the average flow velocity u in the viscous layer is lower in Exp. 3 ($u = \sim 0.6$ mm h⁻¹) than in Exp. 2 ($u = \sim 1.8$ mm h⁻¹; Fig. 11a).

During the post-extensional phase and during the syn-sedimentary phase, viscous flow above the fault tip spreads over a wider zone, if basement extension was slow (Fig. 11a). By contrast, maximum displacement $d_{x\max}$ and flow velocity u in the viscous layer are higher, when basement extension

was rapid (Exp. 2; Fig. 11a) compared to slow basement extension (Exp. 3).

In summary, decreasing the displacement rate of the basement fault e leads to an increased width of the monocline in the cover, a wider zone affected by flow in the viscous layer, but a lower flow velocity in the viscous layer (Fig. 11a).

5.2 Effect of the thickness of the viscous layer h_d

A thicker viscous layer h_d causes a wider and smoother bending of the monoclines above the fault tips (Exp. 5, Fig. 11b). At small h_d (Exp. 4) a cover graben develops adjacent to the basement fault. In Exp. 4, the mature pillow structures are comparatively narrow (~ 6 cm) and are located close to the basement faults. In experiments with larger h_d (Exp. 1a, 5), pillows are wider, their elevation is higher, and the distance to the basement graben is larger (see the Supplement).

The zone affected by viscous flow increases in width in all phases of the experiment, if the thickness of the silicone

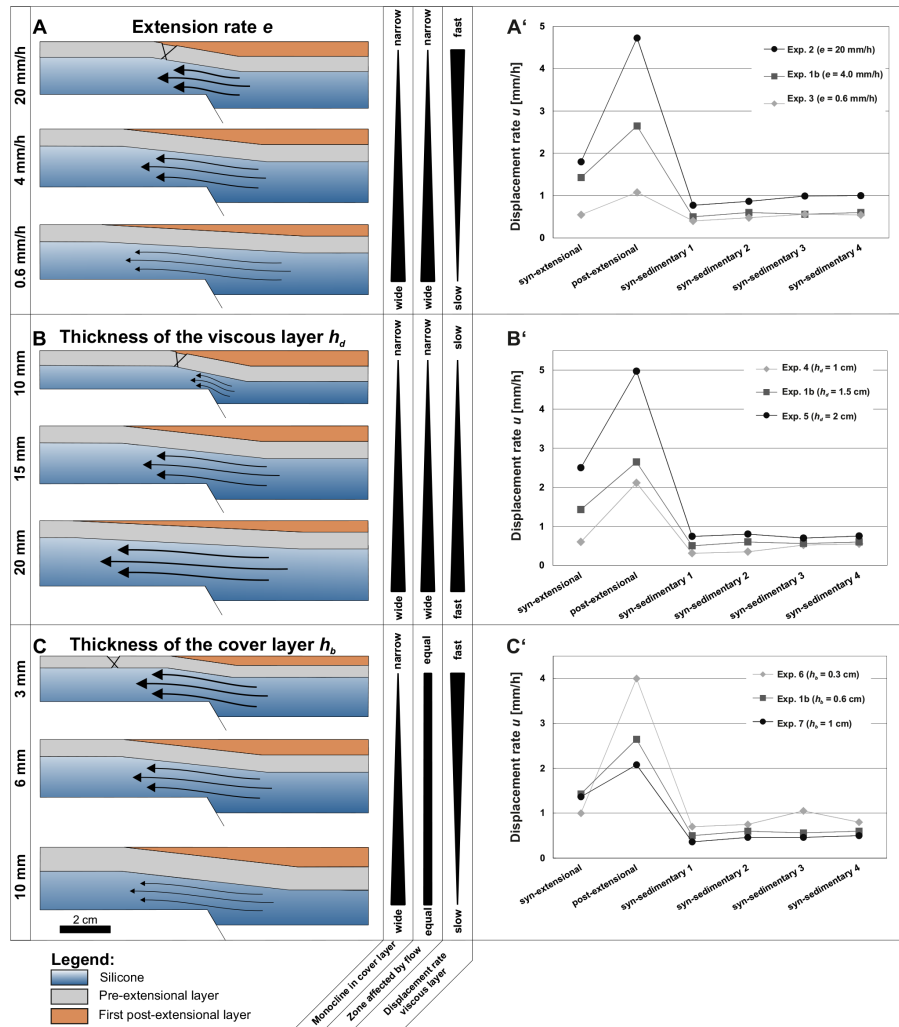


Figure 11. Summarized results of the structures, the kinematics, and the displacement rates u depending on (a/a') extension rate at the basement fault e , (b/b') thickness of the viscous layer h_d , and (c/c') thickness of the cover layer h_b . Black arrows indicate extent of flow in the silicone layer, whereas the thickness of the arrows represents the displacement rates. Triangles and bars in the centre column reflect increasing or decreasing effect on structures and kinematics. The displacement rates are generally highest during the post-extensional phase. During the syn-sedimentary phases, the displacement rates are notably lower. Note that only the values of the first four syn-sedimentary phases are displayed while most experiments last longer.

layer is larger (Exp. 5; Fig. 11b). During basement extension, flow velocities are higher for a thick viscous layer (Exp. 5: $u \sim 2.5 \text{ mm h}^{-1}$) than for a thin viscous layer (Exp. 4: $u \sim 0.7 \text{ mm h}^{-1}$) applying an equal amount of basement extension (Fig. 11b). A similar dependence can be observed for the post-extensional and the syn-sedimentary phase (Exp. 4: $u \sim 0.4 \text{ mm h}^{-1}$; Exp. 1b: $u \sim 0.5 \text{ mm h}^{-1}$; Exp. 5: $u \sim 0.8 \text{ mm h}^{-1}$). Exp. 5 ($h_b = 20 \text{ mm}$; Fig. 11b) shows the highest post-extensional flow velocities of all experiments ($u \sim 5 \text{ mm h}^{-1}$), which even exceeds the actual basement extension rate ($e = 4 \text{ mm h}^{-1}$). Eventually, fast silicone flux leads to an initial active piercing of the silicone through the crest of the pillow structures in this experiment.

5.3 Effect of the thickness of the cover layer h_b

A thicker cover layer h_b (Exp. 1b, 8; Fig. 11c) causes a wider and smoother bending of the monoclines above the fault tips. Compared to this, a narrow monocline occurs if h_b is small (Exp. 6; Fig. 11c). With increasing h_b the pillows become wider and located in a larger distance from the basement graben (see the Supplement). Only if the thickness of the cover is very large ($h_b = 15 \text{ mm}$, Exp. 8), do no distinct pillow structures evolve. In this case, the silicone layer above the footwall block is thickened over a broad area and the sinking of the HPS merely lasts a few syn-sedimentary phases.

Varying h_b has relatively minor effects on flow patterns. In each phase of the experiments, the lateral extent of silicone flow is only slightly wider for larger cover thicknesses (e.g. Exp. 7) compared to experiments with smaller cover thicknesses. Flow velocities u in the viscous layer are roughly similar during the syn-extensional phase, independent of h_b ($u = 1$ to 1.5 mm h^{-1} ; Fig. 11c). During the post-extensional and syn-sedimentary phases, respectively, flow velocities are higher in the experiment with a thinner pre-extensional cover layer (Exp. 6) compared to experiments using a thicker cover layer (Exp. 7, 1a; Fig. 11c).

6 Discussion

6.1 Structural evolution

Our experimental procedure involved a short pulse of basement extension followed by a long-lasting phase of post-extensional sedimentation, which is different from most previous experimental studies (Nalpas and Brun, 1993; Koyi et al., 1993; Dooley et al., 2005). As in experiments by Nalpas and Brun (1993) and Dooley et al. (2005), we can distinguish (1) basement fault-related salt structures and (2) platform salt structures.

1. The basement fault-related salt structures, here referred to as primary pillows, are located close to the basement faults, but entirely on the footwall block. In Fig. 5 we showed that the main depocentres in the HPS gradually migrate from the centre of the sink towards the crests of the rising pillows. This indicates that the viscous material is squeezed beyond the basement fault and that the primary pillows develop further away from the basement fault. This observation is in agreement with most of the previous experimental studies mentioned above, which showed that early stage salt structures or cover grabens are laterally offset from the basement fault tip if a viscous detachment is present (e.g. Withjack and Callaway, 2000).
2. The pillows of the second type (secondary pillows) are located further on the footwall block. In our experiments, decoupled cover faults developed close to the edge of the experimental box, which is likely an effect of the side wall (see below). Secondary pillows mainly grew during later syn-sedimentary phases, when the footwall peripheral sink (FPS) formed. This suggests that the formation of secondary pillows does not depend on layer thinning above the footwall platform. This type of pillow is rather forced by differential loading produced by the peripheral sink of the neighbouring primary pillow. This process is similar to the development of “secondary diapirs” (Warsitzka et al., 2013), which are generated by the subsidence of minibasins adjacent to diapirs (Cobbold et al., 1989; Goteti et al., 2012; Peel,

2014) and which have been exemplarily shown to occur in nature, e.g. in the North German Basin (Strunck et al., 1998).

6.2 Kinematics

Two end member types of flow patterns were observed in our experiments: (1) downward flow above the basement fault tip occurs during the initial phase of extension and the post-extensional phase; (2) subsequently, upward flow occurs during (post-extensional) sediment accumulation in the HPS. We interpret this reversal of flow direction in our experiment as a result of the prevailing gradient of the hydraulic head (e.g. Kehle, 1988; Koyi et al., 1993). Downward flow is driven by elevation head as soon as the viscous layer is vertically displaced. Sand accumulation in the hanging wall peripheral sink creates differential loading. Due to this, a pressure head in the viscous layer induces a reversal of the flow direction. Flow velocities during syn-sedimentary upward flow are small compared to those during downward flow (Fig. 11). Hence, we infer that the pressure head is only slightly higher than the elevation head. During subsequent phases of sedimentation, flow velocities in the viscous layer above the basement fault increase (Fig. 11) denoting a gradually increasing pressure head. During later stages of the experiments, lateral spreading of regions affected by viscous flow across the footwall platform (Fig. 9) suggests that an additional pressure head is imposed above the footwall block. This is due to the subsidence of the FPS. However, the more deeply subsided HPS and the strain patterns (Fig. 9) suggest that the supply of the primary pillow from the footwall side remains minor throughout the experimental evolution. The main portion of viscous material within the primary pillow flows in from the footwall side.

Deformation visualized through vector grids (Figs. 7, 8) suggests that lateral flow of the viscous material equilibrates the vertical movement of the overburden and viscous material is expelled from subsiding towards uplifting regions. Therefore, the flow regime within the viscous layer can be described as squeezed channel flow (e.g. Fuchs et al., 2014), i.e. the idealized parabolic vector profiles (Poiseuille flow) are vertically compressed beneath subsiding areas and vertically extended in regions of material accumulation. Such channel flow occurs in opposite direction to shearing at the basement during the syn-extensional phase (Fig. 6). This indicates that stresses applied by the hydraulic head can exceed shear stress caused by lateral strain. During post-extensional and syn-sedimentary phases, broad regions affected by channel flow were observed above the basement step. This demonstrates that small displacements of the basement ($D_r < 1$) can cause widespread stresses in the viscous layer.

6.3 Sensitivity study

Varying the layer thicknesses and extension rates provides insights into the reliability of the observed material flow patterns and conditions for pillow formation. By increasing the thickness of the viscous layer h_d , a wider region is affected by faster viscous flow. This indicates that frictional forces at the top and the bottom of the viscous layer are less significant in a thick viscous layer than in a thin viscous layer assuming the same hydraulic head. Therefore, the growth of pillows is facilitated if the salt layer is thicker.

In experiments with a thicker cover layer, flow velocities were generally lower and the formation of pronounced pillow structures was suppressed. This results from enhanced normal stresses at the top of the viscous layer, if the overburden is thick. Thus, the resistance against uplift above the footwall block increases and inflow of viscous material from the hanging wall block during the syn-sedimentary phase is impeded. Nevertheless, significant parts of the viscous layer are affected by horizontal material flow during the syn-sedimentary phase, even if the thickness of the cover layer is large (Exp. 8; see the Supplement). This indicates that viscous material accumulated over a larger region leading to subtle, but broad uplifts.

The basement extension rate e affects flow patterns and displacement rates u in the viscous layer during the post-extensional and syn-sedimentary phases. Post-extensional and syn-sedimentary flow velocities were lower after slow basement extension (Exp. 3; Fig. 11), because viscous flow was able to keep pace with the subsidence of the downthrown basement block. Hence, the space created by basement subsidence was partly equilibrated by increasing the thickness of the viscous layer (Jackson et al., 1994; Higgins and Harris, 1997). Fewer syn-kinematic sediment could be added to the hanging wall peripheral sink, which reduced the effect of differential loading. In experiments applying fast basement extension (Exp. 2) high syn-sedimentary flow velocities were observed above the basement fault. This is because the subsidence of the HPS was similar to basement subsidence. Hence, syn-kinematic layers in the HPS are thicker leading to a higher pressure head. Therefore, it can be assumed that fast basement extension promotes post-extensional pillow growth, at least when the displacement of the basement fault was small.

6.4 Limitations of the experimental procedure

All experiments have been set up with a pre-kinematic overburden layer before the onset of basement extension. However, the sensitivity study revealed that flow velocities are higher and pillow structures are larger in experiments with a thinner cover layer. Thus, it can be inferred that without a pre-kinematic cover layer, sand accumulation in the HPS would trigger the formation of a minibasin and nearby down-built diapirs (e.g. Burliga et al., 2012; Goteti et al., 2012).

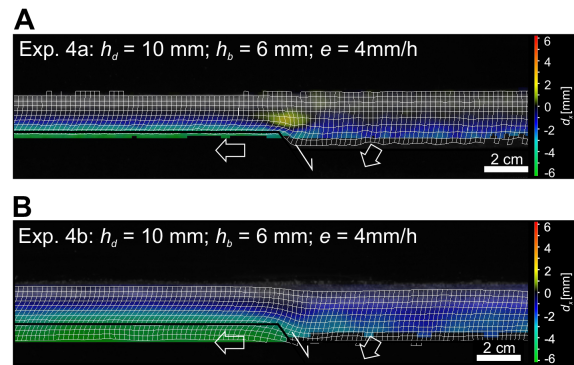


Figure 12. Comparison of two experiments with equal initial conditions, but (a) without syn-extensional sand accumulation and (b) with syn-extensional sand accumulation in the hanging wall peripheral sink. Downward flow is prevented in (b). However, no upward flow can be recognized in (b), although differential loading between the hanging wall side and the footwall side is present. Coloured areas display rightward (yellow–red) and leftward (green–blue) movement of the analogue material.

Decoupled cover grabens and secondary pillows developed close to the edge of the experimental box, where the silicone layer pinches out. In nature there is no comparable lateral confinement of the salt layer. However, irregularities of the basement, above which the thickness of the viscous layer changes, can also determine the location of decoupled thin-skinned extension (e.g. Gaullier et al., 1993). Similarly, secondary pillows can also be caused by a subsiding minibasin in a laterally extended salt layer (e.g. Peel et al., 2014).

Basement displacement and syn-kinematic sediment accumulation were artificially separated in our experiments, although these processes are contemporaneous in nature. In some preliminary experiments, e.g. Exp. 4b, additional sand was sieved into the subsiding HPS during basement extension. In these experiments downward flow above the basement fault was non-existent, but no upward flow was induced during the syn-extensional phase (Fig. 12). This might be due to shearing in the viscous layer above the basement fault, and due to the low density contrast between the viscous material and the cover layer. In other experimental studies simulating salt diapirism due to basement extension (e.g. Burliga et al., 2012; Dooley et al., 2005) syn-extensional sedimentation was applied and no phase of downward flow was described. However, the density of the sand cover in those experiments was $\Delta\rho = 500\text{--}700\text{ kg m}^{-3}$ higher than the density of the viscous layer. This exaggerates the effect of buoyancy and differential loading (Allen and Beaumont, 2012) compared to natural systems – at least for the initial stage of salt structure development.

In nature, overburden density increases due to compaction and exceeds that of salt at depths of 600–1500 m (Jackson and Talbot, 1986). This compaction process is difficult to simulate in analogue models. Assuming a relatively thin

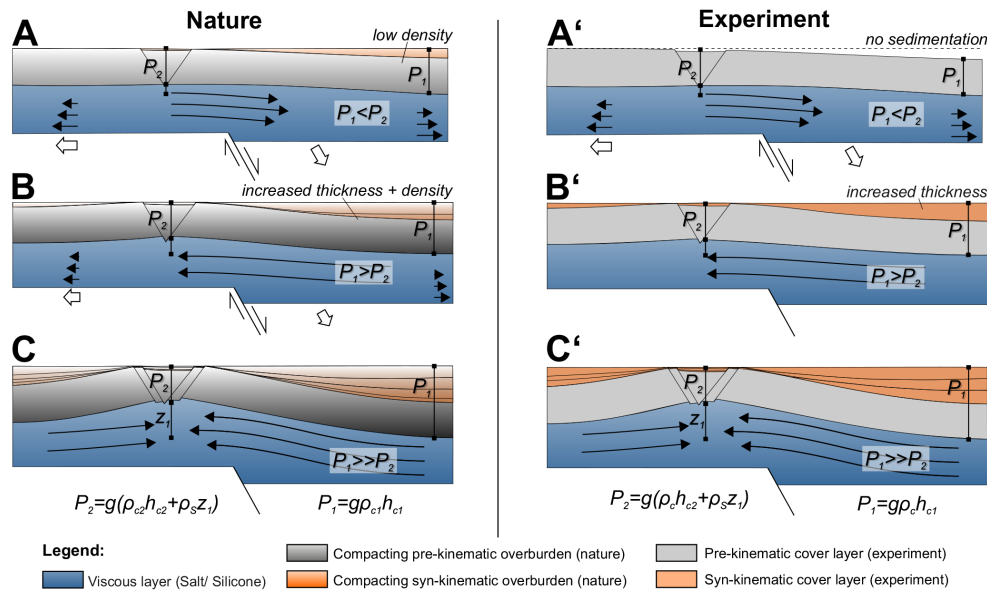


Figure 13. Conceptual model of the formation of a pillow and corresponding flow patterns in nature and experiment. (a) During initiation of basement faulting average density of the overburden in the HPS is still lower than that of salt causing only a low amount of differential loading. (a') This is similar to the lack of sedimentation in the experimental peripheral sinks. In both cases downward flow occurs above the fault tip since the pressure head is smaller than the elevation head. (b) Due to further basement extension, thickness and density of the overburden above hanging wall side increase. (b') Additional cover material is filled into the HPS. In both cases, upward flow above the basement fault is initiated by an increasing pressure head. (c/c') During decreased or stopped extension, the viscous material can continuously flow upward causing the formation of a pillow structure.

pre-kinematic overburden layer (< 1000 m), the average density of the natural overburden is lower than that of salt. However, density increases with burial especially in the hanging wall peripheral sink, where thick sediments are deposited. Therefore, differential loading between a peripheral sink and a nearby salt structure becomes more effective with increasing subsidence of the HPS. For comparison of our experimental results with natural salt tectonics, filling the HPS with additional sand slightly denser than the viscous material is similar to the gradual compaction process in nature during continuous syn-extensional sedimentation (see below). In both cases, the pressure head exceeds the elevation head at a certain amount of subsidence of the HPS (Fig. 13).

6.5 Inferences concerning pillow growth and salt flow in extensional basins

Both components of the hydraulic head (elevation head and pressure head), modelled separately in our experiments, temporally and spatially overlap in natural salt-bearing extensional basins. However, we suggest that as in our models, the elevation head can dominate during early growth stages of natural salt pillows according to the following conceptual model (Fig. 13): at the beginning a viscous layer and its overburden are gradually displaced by basement faulting. As long as the average density of the overburden is smaller than that of salt, differential loading is also small, even if sediment

supply is high enough to keep pace with basement subsidence (Fig. 13a). Hence, early downward flow is driven by elevation head. If basement displacement continues, density of the overburden in the HPS increases due to compaction and, therefore, differential loading becomes more effective. At a certain depth of the HPS, pressure head increases sufficiently to exceed the elevation head and upward flow is induced (Fig. 13b). When this stage is reached, progressive subsidence of the HPS drives further expulsion of the viscous material even if basement extension terminates (Fig. 13c, c'). Consequently, the viscous material accumulates above the higher basement compartment, where the overburden is uplifted. Overall, this is a feasible mechanism explaining salt pillow formation and corresponding peripheral sinks in extensional settings. Other processes may modify the evolution described here, e.g. the accumulation of dense sediment (such as carbonates) in the HPS or erosion of the graben flanks.

Based on our experimental results, we propose the following hypotheses for salt structure evolution in extensional settings:

1. In contrast with previous analogue models (e.g. Dooley et al., 2005; Ge and Vendeville, 1997; Koyi et al., 1993; Nalpas and Brun, 1993), no diapirs evolved in our experiments. Therefore, we suggest that small-offset basement faults ($D_r < 1$) are generally insufficient to trigger reactive piercing of the salt.

2. Furthermore, we suggest that the successful formation of a salt pillow due to basement displacement requires a phase of tectonic quiescence, in which the salt is able to flow upwards and accumulate on the footwall side. As demonstrated by other analogue model studies (e.g. Burliga et al., 2012; Dooley et al., 2005) uninterrupted basement extension leads to enhanced cover faulting and shearing of the viscous material above the basement step. This reduces material supply from the hanging wall side (Burliga et al., 2012), but promotes reactive diapirism above the basement fault tip without the occurrence of a pillow stage.
3. In experiments involving large initial overburden thicknesses (> 1 cm), no distinct pillow structure evolved. Scaled to nature, this implies that pillows are suppressed when the overburden is thicker than ~ 1000–1500 m. This value is only a rough quantitative estimation, since rock properties in nature (e.g. salt viscosity, strength of the overburden) are more variable than in analogue models. Salt pillows showing a particularly thick pre-kinematic overburden layer, e.g. in some parts of the North German Basin (Baldschuhn et al., 2001), were possibly generated by another mechanism than the one simulated in our experiments. Other viable mechanisms include regional tectonic contraction (Kossov and Krawczyk, 2002), the progradation of sedimentary wedges (Ge and Vendeville, 1997) or the formation of a residual elevation between two growing salt structures (Vendeville, 2002).

6.6 Comparison with natural examples

The structural development and kinematics derived from our experiments can be compared to natural examples of salt structures in extensional basins such as the North Sea Basin (Duffy et al., 2013; Korstgård et al., 1993), the Dniepr-Donets Basin (Stovba and Stephenson, 2003), the Lusitanian Basin (Alves et al., 2002), the Mid-Polish Trough (Krzywiec, 2004a; Wagner et al., 2002) or the North German Basin (Baldschuhn et al., 2001; Jaritz, 1987; Kockel, 1998). Cross-sections displayed in Fig. 14 show some examples of these basins. The overburden layers of the peripheral sinks have been reconstructed using vertical simple shear (Rowan and Ratliff, 2012) and line length unfolding in 2-DMove (Midland Valley). Different from our simplified experimental setup, the present-day basement of the salt layer exhibits a complex fault pattern. Nevertheless, differentially subsided basement compartments can be distinguished, which we attribute to differential loading on the salt layer.

The salt pillow exhibited in Fig. 14a developed above a slightly deformed basement. The pillow bears a close resemblance to the experimental pillow structures observed in our analogue models (Fig. 4). Hence, we suggest that such salt pillows were initiated by differential basement subsidence

and continued to grow due to differential loading applied by nearby peripheral sinks.

In cross-section C of the Weser Trough (North German Basin) (Fig. 14c), local thickness variations in the post-salt Middle Buntsandstein (Early Triassic) layer provide evidence for the onset of basement faulting. During a phase of intensified extension in Middle Keuper time (Late Triassic) in the North German Basin (Kockel, 2002; Mohr et al., 2005; Scheck-Wenderoth et al., 2008), the HPS in the Weser Trough had increased in depth and salt pillows evolved. Based on our modelling results, we suggest that the main driving forces for salt flow and pillow formation were differences in loading between the HPS and the locally faulted overburden above the footwall compartments. Small offset basement faults induced widespread expulsion of the salt into relatively broad pillow structures. Due to renewed extension during Late Keuper (Late Triassic) and Early to Middle Jurassic times reactive diapirism took place.

Extension in the Mid-Polish Trough (Fig. 14d) had already begun during Early Triassic or might have continued since Late Permian (Krzywiec, 2004b). For this reason, the pre-kinematic (pre-extensional) overburden above the Upper Permian (Zechstein) salt layer was probably very thin or completely absent. Nevertheless, the reconstruction of cross-section C suggests that no significant pillow formed before the Middle Triassic. According to our conceptual model, the density of the Lower Triassic layers was insufficient to generate significant differential loading and to support an upward directed salt flow at the beginning (Early Triassic). During the Middle Triassic, a second phase of basement extension and compaction of the sediments in the HPS created a pressure head, which was high enough to drive upward flow and pillow uplift. Syn-kinematic sediments in the HPS reveal that the main depocentre migrated towards the left-hand salt structure during the Middle Late Triassic. According to our experimental results this indicates that the salt was progressively expelled towards the footwall block, where it accumulated in the rising Klodawa salt structure. During the Late Triassic, the Klodawa salt structure began to pierce as a diapir due to further basement extension.

Early flow patterns within evolving salt structures cannot be retrieved from seismic interpretations, but can be proposed on the basis of our experimental results and from rare outcrop studies in salt mines. Burliga (1996) interpreted folded salt layers in a salt mine in the Klodawa salt diapir (Mid-Polish Trough) to be a result of different phases of salt flow. During an early stage (Early Triassic) salt flowed downwards towards the basin axis. During the mature stage of the Klodawa diapir, salt moved from the downthrown basement block towards the rising salt structure due to differential loading between the basin centre and the crest of the salt structure (Burliga, 1996). This interpretation is supported by our experimental results and shows how experiments can help to understand the evolution of salt structures and their reconstructions. Furthermore, examples from salt mines in the

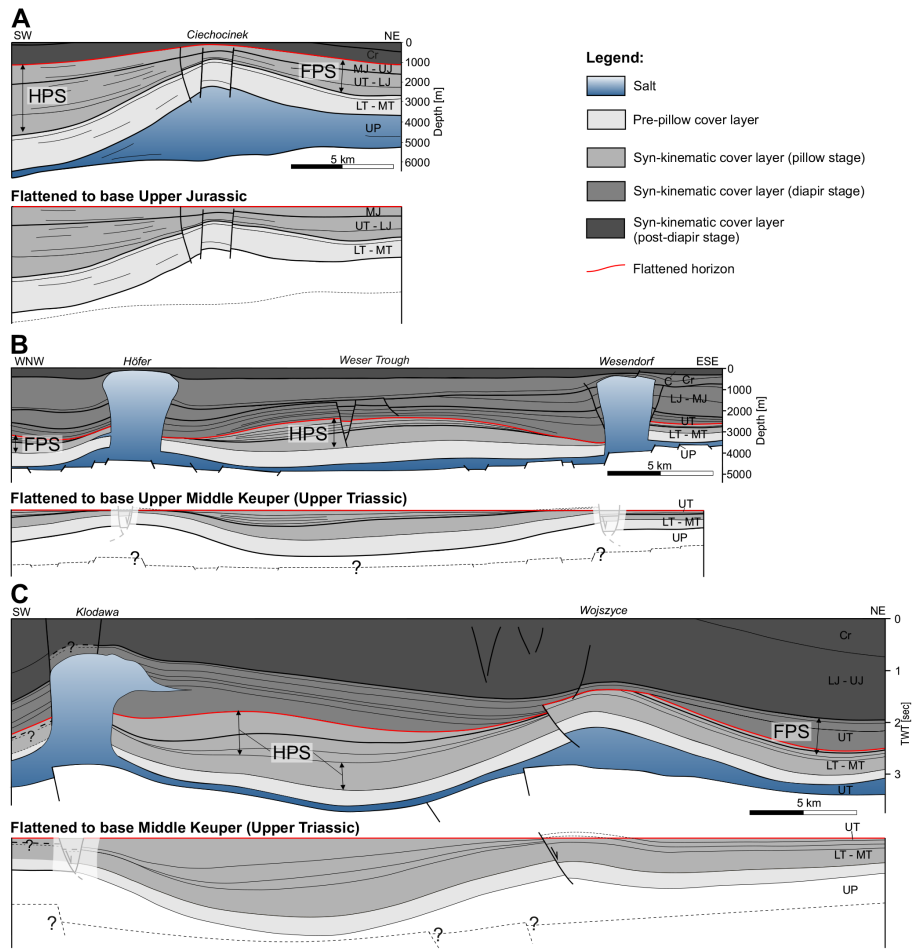


Figure 14. Interpreted seismic profiles of salt structures including reconstruction of the hanging wall peripheral sink (HPS) and the footwall peripheral sink (FPS). The sub-salt basement has not been restored, but its assumed geometry is schematically denoted. **(a)** The cross-section of the Mid-Polish Basin (modified after Dadlez, 2003) shows a typical salt pillow that was probably initiated by differentially subsided basement. In cross-sections **b–c**, the main depocentres overlie the downthrown basement part and salt structures are located above basement highs. **(b)** The Weser Trough (Central North German Basin) experienced several extensional phases during the Mesozoic, which led to the formation of salt pillows during Early Triassic and to diapiric piercing during the Late Triassic (modified from Baldschuhn et al., 2001). **(c)** The salt structures Klodawa and Wojszyce in the Mid-Polish Trough were initiated during the Middle to Late Triassic above a half graben (modified from Krzywiec, 2004b). Late Cretaceous inversion caused strong uplift of the sub-salt basement. UP – Upper Permian; LT – Lower Triassic; MT – Middle Triassic; UT – Upper Triassic, LJ – Lower Jurassic; MJ – Middle Jurassic; UJ – Upper Jurassic, Cr – Cretaceous; C – Cenozoic. For locations of the profiles see references.

North German Basin disclose complex internal folding of the evaporite succession even in regions of less external tectonic imprinting in the basement or the overburden (e.g. Bornemann, 1979; Richter-Bernburg, 1980; Strozyk et al., 2013; van Gent et al., 2010). Flow kinematics in our experiments demonstrate that significant strain in the viscous layer can occur despite only slight deformation of the basement and overburden.

7 Conclusions

Our experimental study simulated flow patterns in a salt layer during a short phase of basement normal faulting followed by a long period of sedimentation and the growth of post-extensional salt pillows.

1. Cross-sections of the final stages of our experiments demonstrate that two types of pillow structure can be distinguished. Primary pillows are located adjacent to basement faults and are mainly driven by differential loading induced by thicker sedimentary layers above the downthrown basement block (hanging wall peripheral

sink). Secondary pillows develop above the footwall block at considerable distance from the basement fault. These pillows are predominantly caused by the subsidence of the peripheral sink flanking the primary pillow on the side facing away from the basement fault (footwall peripheral sink). The sensitivity study revealed that the growth of salt pillows is facilitated by a large thickness of the viscous layer, a small thickness of the overburden and fast basement extension with a small offset of the basement fault.

2. Monitoring the deformation patterns within the analogue materials using PIV reveals that during basement extension, viscous material above the basement fault tip moves downward driven by elevation head. During the syn-sedimentary stage, the pressure head due to differential sedimentary loading forces upward flow. We propose that the downward and subsequent upward flow also occur successively in nature. At the beginning, average density of the overburden is lower than that of salt. Consequently, differential loading is low and the elevation head dominates. During further basement subsidence, syn-kinematic sedimentation and compaction in the hanging wall peripheral sink lead to an increased overburden density. Differential loading increases until the pressure head exceeds the elevation head and upward flow is induced. Viscous material is now squeezed out from beneath the hanging wall peripheral sink to form pillow-like structures on the footwall side. During further post-extensional phases, an additional pressure head is applied due to the development of a peripheral sink above the footwall block. This initiates the growth of the secondary pillow.
3. The flow regime in the viscous material can be mainly characterized as squeezed channel flow. Subsidence and uplift of the overburden are spatially correlated with expulsion or inflation of the viscous material. Compared to focused, small displacements at the basement faults, the region affected by viscous flow is widespread and widens further during post-extensional sedimentation. As shown by the sensitivity study, strain patterns in the viscous layer are basically independent of layer thicknesses or displacement rates. However, the zone affected by viscous flow above the fault tip is wider if the ductile layer is thicker, or if the basement displacement rate is smaller. Flow velocities in the viscous layer above the basement fault tip are higher if the ductile layer is thicker, if the overburden layer is thinner, or if the basement displacement rate is higher.
4. The comparison of our experimental results with natural salt-bearing extensional basins demonstrates the similarity of structural geometries, e.g. hanging wall peripheral sinks surrounded by pre-diapiric salt pillows. Despite the limitations of the experimental set-up, e.g. simple basement geometry or the temporal separation between extension and sedimentation, our experimental procedure provides a generic model for the early evolution of salt structures in basins that experienced multiple extensional phases followed by post-extensional thermal subsidence.

Appendix A

A1 Frictional-plastic material behaviour

The mechanical behaviour of granular material like sand is described by the coefficient of internal friction μ and the cohesion C (Lohrmann et al., 2003). These material properties were measured in two-cycle dynamic friction tests at variable normal loads and variable shear rates with the ring-shear tester RST-01.pc (Schulze, 1994). During a first shear load cycle, peak friction was determined. This defines the strength during material failure and shear zone formation. In a second shear load cycle, the static stable frictional strength was measured. This represents the strength during reactivation of shear zones within the material. Following material failure after exceeding peak strength or static stable strength, respectively, a constant dynamic-stable strength in a stage of ongoing fault activity is reached (Panien et al., 2006).

The values of average frictional properties and bulk density of the materials used in our experiments are listed in Table A1. Similar to our experimental procedure sand was sifted in the measurements of the ring shear tests to achieve optimal grain package (Lohrmann et al., 2003). The variability of densities of the sifted granular materials is of the order of $\Delta\rho = 30 \text{ kg m}^{-3}$. Accuracy of the estimation of cohesion is quite low ($\sim 50\%$). Due to electrostatic forces, the cohesions between PVC beads might be significantly higher, especially under tension. Nevertheless, the mixture of PVC beads and quartz sand visibly reduces electrostatic accumulation of the particles.

A2 Viscoelastic material behaviour

The silicone oil (Polydimethylsiloxane; Momentive Performance Materials Baysilone[®] SE30) used in our experiments is characterized by a power-law viscous rheology. In creep and relaxation tests a low power-law stress exponent of $n = 1.3$ had been determined by Rosenau et al. (2009) for the same silicone material used in our study. Additionally, we measured the viscosity with a cone-plate rheometer RC20.1-CPS-P1 with C25-2 measurement system (RheoTec). During measurement a thin film of silicone is sheared between the plates of the rheometer at controlled shear rates and room temperature (20 °C). The viscosity is calculated as the ratio of measured shear stress and strain rate. The thickness of the silicone film was increased stepwise from 1 to 3 mm. Measurements were repeated three times for each thickness. Average values for viscosity are listed in Table A2.

In order to record material movement with PIV, the transparent silicone was mixed with PVC beads. The viscosity of the mixed silicone is only slightly higher ($\Delta\eta = 240 \text{ Pas}$) than that of pure silicone (Table A2). The bulk density of the mixed silicone remains unaffected since the PVC beads possess a similar grain density compared to the density of pure silicone.

Appendix B

To ensure the significance of experimental results, experiments have to be properly scaled geometrically, kinematically and dynamically. Models are considered as geometrically scaled if ratios of linear dimensions in the model are proportionally similar to length ratios in nature (Hubbert, 1937). We used a length ratio l^* between model and nature of 10^{-5} (1 cm in the model corresponds to 1 km in nature), which is derived from the ratio of cohesion of the brittle cover (e.g. Koyi et al., 1993; Nalpas and Brun, 1993; Vendeville et al., 1995; Weijermars et al., 1993):

$$l^* = (C_0/g\rho)^* \quad (\text{B1})$$

in which C_0 is the cohesion, g the gravitational acceleration, ρ the density and $*$ represents the ratio between model and nature. Kinematic scaling is achieved if the ratios between strain and time are similar for model and nature (Hubbert, 1937). The time ratio considers the viscosity ratio η^* between the silicone and the rock salt and the stress ratio σ^* (Table 1):

$$t^* = (\eta^*/\sigma^*). \quad (\text{B2})$$

Since we simulate a tensile stress regime, lithostatic pressure is the main principal stress (Twiss and Moores, 1992):

$$\sigma_N = g \cdot \rho_b \cdot h_b, \quad (\text{B3})$$

where g is the gravitational acceleration, ρ_b the bulk density and h_b the thickness of the salt cover layer. Implying values for viscosities, length and density of Table 1, the time ratio becomes $t^* = \sim 1.3 \times 10^{-9}$. Consequently, 1 h in experiments equals approximately 1 Ma. The strain rate ratio ε^* ($\varepsilon_m/\varepsilon_n$) is the inverse of time ratio $1/t^*$.

In order to fulfil dynamic scaling, the strength ratio between brittle cover S_b and ductile layer S_d has to be equal for nature and experiment (Weijermars et al., 1993). S_b equals the differential stress between maximum and minimum principal stresses:

$$S_b = \sigma_1 - \sigma_3. \quad (\text{B4})$$

As mentioned above, the maximal principal stress σ_1 equals the overburden pressure due to gravity σ_N , whereas the minimal principal stress σ_3 is horizontal and in direction of extension. Both natural sediment and granular analogue material are supposed to deform according to the Mohr–Coulomb failure criterion which is given by (Byerlee, 1978; Dahlen, 1990)

$$\tau_m = \sigma_m \sin\phi + C_0 \cos\phi \quad (\text{B5})$$

in which σ_m = normal stress, τ_m = shear stress, ϕ is the angle of internal friction and C_0 the cohesion. Translating to an expression of maximum and minimum stresses gives

$$\frac{\sigma_1 - \sigma_3}{2} = \frac{\sigma_1 + \sigma_3}{2} \sin\phi + C_0 \cos\phi. \quad (\text{B6})$$

Table A1. Material parameters (density ρ , coefficient of internal friction μ and the cohesion C) of used granular material measured with ring shear tester RST-01.pc.

Material	Grain size [mm]	Preparation	peak ρ [kg m^{-3}]	Peak μ	Peak C [Pa]	Stable static μ	Stable Static C [Pa]	Stable dynamic μ	Stable dynamic C [Pa]
PVC beads	0.36–0.5	sifted	750 ± 10	0.33 ± 0.006	109 ± 44	0.32 ± 0.003	119 ± 25	0.34 ± 0.030	121 ± 196
Quartz sand G23	0.02–0.63	sifted	1740 ± 17	0.70 ± 0.008	88 ± 45	0.61 ± 0.005	92 ± 36	0.55 ± 0.002	103 ± 10
Mixture PVC : quartz sand 1 : 1	0.02–0.63	sifted	1250 ± 10	0.51 ± 0.006	107 ± 44	0.50 ± 0.003	72 ± 25	0.45 ± 0.030	72 ± 196

Table A2. Physical properties of silicone putty used in the study presented here.

Material	Weight of sand added to silicone [kg]	Density ρ [kg m^{-3}]	Strain rate ε [s^{-1}]	Shear stresses τ [Pa]	Viscosity η [Pa s]
Silicone PDMS	0	970	0.01–0.08	< 2000	23000 ± 1000
Silicone PDMS mixed with sand	0.01–0.03	970	0.01–0.08	< 2000	23240 ± 1000

With separation of σ_3 , one obtains

$$\sigma_3 = -\sigma_1 \frac{(1 - \sin \phi)}{(1 + \sin \phi)} + 2C_0 \sqrt{\frac{(1 - \sin \phi)}{(1 + \sin \phi)}}. \quad (\text{B7})$$

Finally, brittle strength S_b can be expressed by

$$S_b = \sigma_1 + \sigma_1 \frac{(1 - \sin \phi)}{(1 + \sin \phi)} - 2C_0 \sqrt{\frac{(1 - \sin \phi)}{(1 + \sin \phi)}}. \quad (\text{B8})$$

For upper crustal rocks, a suitable value for angle of internal friction is $\phi = 30^\circ$ and for cohesion is $C_0 = 5 \times 10^6$ Pa (Byerlee, 1978). Generally, density of clastic sediments usually exceeds the density of rock salt (of $\rho_{\text{Salt}} = 2200 \text{ kg m}^{-3}$) at depths of 650 to 1500 m (Baldwin and Butler, 1985). Assuming a pre-kinematic cover thickness of $h_b = 1000$ m we applied a cover density of $\rho_b = 2300 \text{ kg m}^{-3}$ for the calculation (Baldwin and Butler, 1985). Therefore, $\sigma_N = \sigma_1 = 2.26 \times 10^7$ Pa and $\sigma_3 = 0.297 \times 10^7$ Pa. Hence, the brittle yield strength at the base is S_b (nature) = 1.96×10^7 Pa.

The mixture of quartz sand and PVC beads possesses a slightly lower angle of internal friction ($\phi = \sim 27^\circ$). The density contrast between granulate and silicone ($\Delta\rho = 300 \text{ kg m}^{-3}$) is only slightly higher than the natural salt-cover density contrast, which is an advance compared to previous analogue models using pure quartz sand ($\Delta\rho = 500\text{--}700 \text{ kg m}^{-3}$). Using values of Table 1 S_b (model) = 60–160 Pa.

Shear stresses in a Newtonian fluid can be calculated by (Turcotte and Schubert, 2014)

$$S_d = \eta \left(u / \frac{1}{2} h_d \right) \quad (\text{B9})$$

in which η is dynamic viscosity, u the displacement rate and h_d the thickness of the viscous layer. The extension rate for continental rifting varies between 0.1 and 1 mm a^{-1} (Allen and Allen, 2005), which gives strain rates in the viscous layer of $\varepsilon = 10^{-14}$ to 10^{-15} s^{-1} for a salt thickness

of 2000 m. Assuming an average viscosity for natural rock salt of $\eta = 10^{18} \text{ Pa s}$ (Nalpas and Brun, 1993; van Keken et al., 1993) and a salt thickness of 2000 m, S_d (nature) = $10^4\text{--}10^5$ Pa.

In our experiments, the displacement rate of the simulated basement extension is $e = 4 \text{ mm h}^{-1}$ (except for one experiment with $e = 0.6 \text{ mm h}^{-1}$ and another experiment with $e = 20 \text{ mm h}^{-1}$, Table 2). Consequently, strain rates in the viscous layer reach values of $\varepsilon = \sim 10^{-5} \text{ s}^{-1}$. Incorporating a silicone layer of a thickness of $h_d = 1.5 \text{ cm}$ and a viscosity of $\eta = 2.3 \times 10^4 \text{ Pa s}$, S_d (model) = ~ 1 Pa.

The dimensionless strength ratios are calculated by

$$S_b/S_d(\text{nature}) = \sim 100\text{--}1000 \quad (\text{B10})$$

and

$$S_b/S_d(\text{model}) = 50\text{--}180. \quad (\text{B11})$$

The model ratio lies within the lower range of the natural ratio. Hence, the models can be taken as dynamically scaled.

The Supplement related to this article is available online at doi:10.5194/se-15-9-2015-supplement.

Acknowledgements. This experimental study was funded by the German Research Foundation (DFG). Additional funding for Michael Warsitzka came from the Federal Ministry of Education and Research (BMBF) (grant Nr. 03IS2091A INFLUINS). Experiments and measurements of material properties were carried out at the Helmholtz Centre Potsdam GFZ German Research Centre for Geosciences. We thank the GFZ technicians for assistance in the laboratory as well as M. Rosenau, M. Scheck-Wenderoth, C. von Nicolai and F. Jähne for constructive discussions. The authors gratefully acknowledge the critical reviews by C. J. Talbot, P. Krzywiec and an anonymous reviewer that significantly improved this paper.

Edited by: F. Rossetti

References

- Adam, J., Urai, J. L., Wieneke, B., Oncken, O., Pfeiffer, K., Kukowski, N., Lohrmann, J., Hoth, S., van der Zee, W., and Schmatz, J.: Shear localisation and strain distribution during tectonic faulting – new insights from granular-flow experiments and high-resolution optical image correlation techniques, *J. Struct. Geol.*, 27, 283–301, doi:10.1016/j.jsg.2004.08.008, 2005.
- Allen, P. A. and Allen, J. R.: *Basin Analysis Principles & Applications*, (Blackwell Science), 2nd edition, pp. 451, 2005.
- Allen, J. and Beaumont, C.: Impact of inconsistent density scaling on physical analogue models of continental margin scale salt tectonics, *J. Geophys. Res.*, 17, 1–22, doi:10.1029/2012JB009227, 2012.
- Alves, T. M., Gawthorpe, R. L., Hunt, D. W., and Monteiro, J. H.: Jurassic tectono-sedimentary evolution of the Northern Lusitanian Basin (offshore Portugal), *Mar. Petrol. Geol.*, 19, 727–754, doi:10.1046/j.1365-2117.2003.00202.x, 2002.
- Baldschuhn, R., Binot, F., Frisch, U., and Kockel, F.: *Geotektonischer Atlas von Nordwest-Deutschland und dem deutschen Nordsee-Sektor - Strukturen, Strukturentwicklung, Paläogeographie* (Tectonic Atlas of Northwest Germany and the German North Sea Sector): *Geologisches Jahrbuch A 153*, 3 CD-ROM, 88 pp., 2001.
- Baldwin, B. and Butler, C. O.: Compaction curves: *AAPG Bull.*, 69, 622–626, 1985.
- Bornemann O.: *Das Gefügeinventar nordwestdeutscher Salzstrukturen in Abhängigkeit von ihrer halokinetischen Stellung*, Universität Braunschweig, Dissertationen, Braunschweig, 1–119, 1979.
- Boutelier, D., Schrank, C., and Cruden, A.: Power-law viscous materials for analogue experiments: New data on the rheology of highly-filled silicone polymers, *J. Struct. Geol.*, 30, 341–353, doi:10.1016/j.jsg.2007.10.009, 2008.
- Burliga, S.: Implications for early basin dynamics of the Mid-Polish Trough from deformational structures within salt deposits in central Poland, *Geol. Quart.*, 40, 185–202, 1996.
- Burliga, S., Koyi, H. A., and Chemia, Z.: Analogue and numerical modelling of salt supply to a diapiric structure rising above an active basement fault, edited by: Alsop, G. I., Archer, S. G., Hartley, A. J., Grant, N. T., and Hodgkinson, R.: *Salt Tectonics, Sediments and Prospectivity*, *Geol. Soc. Spec. Publ.*, 363, 395–408, doi:10.1144/SP363.18, 2012.
- Byerlee, J. D.: *Friction of Rocks*, edited by: Byerlee, J. D. and Wyss, M., in: *Pure and Applied Geophysics, Contribution to Current Research in Geophysics*, 116, 615–626, 1978.
- Cobbold, P., Rossello, E., and Vendeville, B.: Some experiments on interacting sedimentation and deformation above salt horizons, *B Soc. Bull. Fr.*, 3, 453–460, doi:10.2113/gssgfbull.V.3.453, 1989.
- Dadlez, R.: Mesozoic thickness pattern in the Mid-Polish Trough, *Geol. Q.*, 47, 223–240, 2003.
- Dahlen, F. A.: Critical Taper Model of Fold-and-Thrust Belts and Accretionary Wedges, *Ann. Rev. Earth Pl. Sc.*, 18, 55–99, doi:10.1146/annurev.ea.18.050190.000415, 1990.
- Dooley, T. P., McClay, P. R., and Pascoe, R.: 3-D analogue models of variable displacement extensional faults: applications to the Revfallet Fault system, offshore mid-Norway, *Geol. Soc. Spec. Publ.*, 212, 151–167, doi:10.1144/GSL.SP.2003.212.01.10, 2003.
- Dooley, T. P., McClay, K. R., Hempton, M., and Smit, D.: Salt tectonics above complex basement extensional fault systems: results from analogue modeling, edited by: Doré, A. G. and Vining, B. A., *Petroleum Geology: North-West Europe and Global Perspectives*, Proceedings of the 6th Petroleum Geology Conference, Geological Society, London, 1631–1648, doi:10.1144/0061631, 2005.
- Duffy, O. B., Gawthorpe, R. L., Docherty, M., and Brocklehurst, S. H.: Mobile evaporite controls on the structural style and evolution of rift basins: Danish Central Graben, North Sea, *Basin Res.*, 25, 310–330, doi:10.1111/bre.12000, 2013.
- Frisch, U. and Kockel, F.: Quantification of Early Cimmerian movements in NW-Germany, *Zbl. Geo. Pal.*, 7–8, 571–600, 1999.
- Fuchs, L., Koyi, H., and Schmeling, H.: Numerical modeling on progressive internal deformation in down-built diapirs, *Tectonophysics*, 632, 111–122, doi:10.1016/j.tecto.2014.06.005, 2014.
- Gaullier, V., Brun, J. P., and Lecanu, H.: Raft tectonics: the effects of residual topography below a salt décollement, *Tectonophysics*, 228, 363–381, doi:10.1016/0040-1951(93)90349-O, 1993.
- Ge, H. and Vendeville, B. C.: Influence of active subsalt normal faults on the growth and location of suprasalt structures, *Gulf Coast Association of Geological Societies Transactions*, XLVII, 169–176, 1997.
- Geil, K.: The development of salt structures in Denmark and adjacent areas: the role of basin floor dip and differential pressure, *First Break*, 9, 467–483, doi:10.3997/1365-2397.1991022, 1991.
- Goteti, R., Ings, S. J., and Beaumont, C.: Development of salt minibasins initiated by sedimentary topographic relief, *Earth Plant. Sc. Lett.*, 339, 103–116, doi:10.1016/j.epsl.2012.04.045, 2012.
- Higgins, R. I. and Harris, L. B.: The effect of cover composition on extensional faulting above re-activated basement faults: results from analogue modelling, *J. Struct. Geol.*, 19, 89–98, doi:10.1016/S0191-8141(96)00083-1, 1997.
- Hubbert, M. K.: Theory of scale models as applied to the study of geologic structures, *Geol. Soc. Am. Bull.*, 48, 1459–1520, 1937.

- Hudec, M. R. and Jackson, M. P. A.: Terra infirma: Understanding salt tectonics, *Earth Sc. Reviews*, 82, 1–27, doi:10.1016/j.earscirev.2007.01.001, 2007.
- Jackson, M. P. A. and Talbot, C. J.: External shapes, strain rates, and dynamics of salt structures, *Geol. Soc. Am. Bull.*, 97, 305–323, doi:10.1130/0016-7606(1986)97<305:ESSRAD>2.0.CO;2, 1986.
- Jackson, M. P. A. and Vendeville B. C.: Regional extension as a geologic trigger for diapirism, *Geol. Soc. Am. Bull.*, 94, 57–73, doi:10.1130/0016-7606(1994)106<0057:REAAGT>2.3.CO;2, 1994.
- Jackson, M. P. A., Vendeville, B. C., and Schultz-Ela, D. D.: Structural Dynamics of Salt Systems, *Ann. Rev. Earth Pl. Sc.*, 22, 93–117, doi:10.1146/annurev.earth.22.050194.000521, 1994.
- Jaritz, W.: The origin and development of salt structures in Northwest Germany, edited by: Lerche, I. and O’Brian, J. J., *Dynamical Geology of Salt and Related Structures*: Academic Press, Orlando, FL, 479–493, 1987.
- Kehle, R. O.: The origin of salt structures, edited by: Schreiber, B. C., in: *Evaporites and Hydrocarbons*, Columbia University Press, New York, 345–404, 1988.
- Kockel, F.: Salt problems in NW-Germany and the German North Sea Sector, *J. Seism. Explor.*, 7, 219–235, 1998.
- Kockel, F.: Rifting processes in NW-Germany and the German North Sea Sector, *Neth. J. Geosci.-Geol. Mijnbouw*, 81, 149–158, 2002.
- Korstgård, J. A., Lerche, I., Mogensen, T. E., and Thomsen, R. O.: Salt and fault interactions in the northeastern Danish Central Graben: observations and inferences, *Bull. Geol. Soc. Den.*, 40, 197–255, 1993.
- Kossow, D. and Krawczyk, C. M.: Structure and quantification of processes controlling the evolution of the inverted NE-German Basin, *Mar. Petrol. Geol.*, 19, 601–618, doi:10.1016/S0264-8172(02)00032-6, 2002.
- Koyi, H. A. and Petersen, K.: Influence of basement faults on the development of salt structures in the Danish Basin, *Mar. Petrol. Geol.*, 10, 82–94, doi:10.1016/0264-8172(93)90015-K, 1993.
- Koyi, H. A., Jenyon, M. K., and Petersen, K.: The effect of basement faulting on diapirism, *J. Petrol. Geol.*, 163, 285–311, doi:10.1111/j.1747-5457.1993.tb00339.x, 1993.
- Krzywiec, P.: Basement vs. salt tectonics and salt-sediment Interaction – case study of the Mesozoic evolution of the Intracontinental Mid-Polish Trough, In 24th Annual GCSSEPM Foundation Bob F. Perkins Research Conference Salt-Sediment Interactions and Hydrocarbon Prospectivity: Concepts, Applications and Case Studies for the 21st Century, Houston, Texas, 343–370, 2004a.
- Krzywiec, P.: Triassic evolution of the Klodawa salt structure: basement-controlled salt tectonics within the Mid-Polish Trough (Central Poland), *Geol. Quart.*, 48, 123–134, 2004b.
- LaVision, Anon.: StrainMaster Manual for DaVis 6.2. LaVision GmbH, Goettingen, 154 pp., 2002.
- Lohrmann, J., Kukowski, N., Adam, J., and Oncken, O.: The impact of analogue material parameters on the geometry, kinematics, and dynamics of convergent sand wedges, *J. Struct. Geol.*, 25, 1691–1711, doi:10.1016/S0191-8141(03)00005-1, 2003.
- Maystrenko, Y. P., Bayer, U., and Scheck-Wenderoth, M.: Salt as a 3-D element in structural modeling – Example from the Central European Basin System, *Tectonophysics*, 591, 62–82, doi:10.1016/j.tecto.2012.06.030, 2013.
- Mohr, M., Kukla, P. A., Urai, J. L., and Bresser, G.: Multi-phase salt tectonic evolution in NW Germany: seismic interpretation and retro-deformation, *Int. J. Earth Sci.*, 94, 917–940, doi:10.1007/s00531-005-0498-8, 2005.
- Nalpas, T. and Brun, J. P.: Salt flow and diapirism related to extension at crustal scale, *Tectonophysics*, 228, 349–362, doi:10.1016/0040-1951(93)90348-N, 1993.
- Oudmayer, B. C. and de Jager, J.: Fault reactivation and oblique-slip in the Southern North Sea, edited by: Parker, J. R., in: *Petroleum Geology of Northwest Europe: Proceedings of the 4th Conference, Petroleum Geology ’86 Ltd.*, Published by The Geological Society, London, 1281–1290, doi:10.1144/0041281, 1993.
- Panien, M., Schreurs, G., and Pfiffner, A.: Mechanical behaviour of granular materials used in analogue modelling: insights from grain characterisation, ring-shear tests and analogue experiments, *J. Struct. Geol.*, 28, 1710–1724, doi:10.1016/j.jsg.2006.05.004, 2006.
- Peel, F. J.: How do salt withdrawal minibasins form?, Insights from forward modelling, and implications for hydrocarbon migration, *Tectonophysics*, 630, 222–235, doi:10.1016/j.tecto.2014.05.027, 2014.
- Ramberg, H.: *Gravity Deformation and the Earth’s Crust*, 1st Ed., Academic Press, London, 452 pp., 1967.
- Rommelts, G.: Fault-related tectonics in the Southern North Sea, The Netherlands, edited by: Jackson, M. P. A., Roberts, D. G., and Snelson, S., in: *Salt Tectonics: A Global Perspective*, AAPG Memoir, 65, 261–272, 1995.
- Richard, P.: Experiments on faulting in a two-layer cover sequence overlying a reactivated basement fault with oblique-slip, *J. Struct. Geol.*, 13, 459–469, doi:10.1016/0191-8141(91)90018-E, 1991.
- Richter-Bernburg, G.: Salt tectonics, interior structures of salt bodies, *Bull. Cent. Rech. Explor.-Prod. Elf-Aquitaine*, 4, 373–393, 1980.
- Rosenau, M., Lohrmann, J., and Oncken, O.: Shocks in a box: An analog model of subduction earthquake cycles with application to seismotectonic forearc evolution, *J. Geophys. Res.*, 114, 1978–2012, doi:10.1029/2008JB005665, 2009.
- Rowan, M. G. and Ratliff, R. A.: Cross-section restoration of salt-related deformation: Best practices and potential pitfalls, *J. Struct. Geol.*, 41, 24–37, doi:10.1016/j.jsg.2011.12.012, 2012.
- Scheck, M., Bayer, U., and Lewerenz, B.: Salt movements in the Northeast German Basin and its relation to major post-Permian tectonic phases – results from 3-D structural modelling, back-stripping and reflection seismic data, *Tectonophysics*, 361, 277–299, doi:10.1016/S0040-1951(02)00650-9, 2003.
- Scheck-Wenderoth, M., Maystrenko, Y. P., Hübscher, C., Hansen, M., and Mazur, S.: Dynamics of salt basins, edited by: Littke, R., Bayer, U., and Gajewski, D. in: *Dynamics of complex intracontinental basins: The Central European Basin System*, *Frontiers in Earth Science*, Springer, Berlin, 307–322, 2008.
- Schultz-Ela, D. D. and Jackson, M. P. A.: Relation of subsalt structures to suprasalt structures during extension, *AAPG Bull.*, 80, 1896–1923, 1996.
- Schulze, D.: Entwicklung und Anwendung eines neuartigen Ringschergerätes, *Aufbereitungstechnik*, 35, 524–535, 1994.

- Soto, R., Casas-Sainz, A., and Del Río, P.: Geometry of half-grabens containing a mid-level viscous décollement, *Basin Research*, 19, 437–450, doi:10.1111/j.1365-2117.2007.00328.x, 2007.
- Stephansson, O.: Theoretical and experimental studies of diapiric structures on Öland, *Geol. Inst. Bull. Univ. Uppsala N. S.*, 3, 163–200, 1972.
- Stewart, S. A., Harvey, M. J., Otto S. C., and Weston, P. J.: Influence of salt on fault geometry: examples from the UK salt basins, *Geol. Soc. Spec. Publ.*, 100, 175–202, doi:10.1144/GSL.SP.1996.100.01.12, 1996.
- Stovba, S. M. and Stephenson, R. A.: Style and timing of salt tectonics in the Dniepr-Donets Basin (Ukraine): implications for triggering and driving mechanisms of salt movement in sedimentary basins, *Mar. Petrol. Geol.*, 19, 1169–1189, doi:10.1016/S0264-8172(03)00023-0, 2003.
- Strozyk, F., van Gent, H., Urai, J. L., and Kukla, P. A.: 3-D seismic study of complex intra-salt deformation: an example from the Upper Permian Zechstein 3 stringer in the western Dutch offshore, *Geol. Soc. Spec. Publ.*, 363, 489–501, doi:10.1144/SP363.23, 2013.
- Strunck, P., Gaupp, R., and Steffan, M.: Early Triassic movement of Upper Permian (Zechstein) salt in Northwest Germany, *Z Geol Paläont Teil*, 1, Heft 7–8, 679–699, 1998.
- Turcotte, D. L. and Schubert, G.: *Geodynamics*, Cambridge University Press, Cambridge, United Kingdom, 3rd edition, 636 pp., 2014.
- Twiss, R. J. and Moores, E. M.: *Structural Geology*, W. H. Freeman and Company, Oxford, 532 pp., 1992.
- Urai, J., Schléder, Z., Spiers, C., and Kukla, P.: Flow and transport properties of salt rocks, in: *Dynamics of Complex Intracontinental Basins: The Central European Basin System*, edied by: R. Littke, U. Bayer, D. Gajewski, S., and Nelskamp, 291–304, Springer, Berlin Heidelberg, 2008.
- Van Gent, H., Urai, J. L., and de Keijzer, M.: The internal geometry of salt structures – A first look using 3-D seismic data from the Zechstein of the Netherlands, *J. Struct. Geol.*, 33, 1–20, doi:10.1016/j.jsg.2010.07.005, 2010.
- Van Keken, P. E., Spiers, C. J., van den Berg, A. P., and Muzyert, E. J.: The effective viscosity of rock salt: implementation of steady-state creep laws in numerical models of salt diapirism, *Tectonophysics*, 225, 457–476, doi:10.1016/0040-1951(93)90310-G, 1993.
- van Wees, J.-D., Stephenson, R. A., Ziegler, P. A., Bayer, U., McCann, T., Dadlez, R., Gaupp, R., Narkiewicz, M., Bitzer, F., and Scheck, M.: On the origin of the Southern Permian Basin, Central Europe, *Mar. Petrol. Geol.*, 17, 43–59, doi:10.1016/S0264-8172(99)00052-5, 2000.
- Vendeville, B. C.: Scale models of basement-induced extension: *Comptes Rendus de l'Academie des Sciences de Paris* 307, 2, 1013–1019, 1988.
- Vendeville, B. C.: A new Interpretation of Trusheim's classic Model of Salt-Diapir-Growth, *Gulf Coast Association of Geological Societies Transactions*, 52, 953–952, 2002.
- Vendeville, B. C. and Jackson, M. P. A.: The rise of diapirs during thin-skinned extension, *Mar. Petrol. Geol.*, 9, 331–353, doi:10.1016/0264-8172(92)90047-I, 1992.
- Vendeville, B. C., Ge, H., and Jackson, M. P. A.: Scale models of salt tectonics during basement-involved extension, *Petrol. Geosci.*, 1, 179–183, doi:10.1144/petgeo.1.2.179, 1995.
- Ventisette, C. D., Montanari, D., Bonini, M., and Sani, F.: Positive fault inversion triggering “intrusive diapirism”: an analogue modelling perspective, *Terra Nova*, 17, 478–485, doi:10.1111/j.1365-3121.2005.00637.x, 2005.
- Wagner, R., Leszczyński, K., Pokorski, J., and Gumulak, K.: Palaeotectonic cross-sections through the Mid-Polish Trough, *Geol. Q.*, 46, 293–306, 2002.
- Warsitzka, M., Kley, J., and Kukowski, N.: Salt diapirism driven by differential loading – Some insights from analogue modelling, *Tectonophysics*, 591, 83–97, doi:10.1016/j.tecto.2011.11.018, 2013.
- Weijermars, R., Jackson, M. P. A., and Vendeville, B. C.: Rheological and tectonic modeling of salt provinces, *Tectonophysics*, 217, 143–174, doi:10.1016/0040-1951(93)90208-2, 1993.
- Withjack, M. O. and Callaway, S.: Active normal faulting beneath a salt layer: an experimental study of deformation patterns in the cover sequence, *AAPG Bull.*, 84, 627–651, 2000.
- Ziegler, P. A.: Triassic Rifts and Facies Patterns in Western and Central Europe, *Geol. Rundsch.*, 71, 747–772, doi:10.1007/BF01821101, 1982.